



48TH TURBOMACHINERY & 35TH PUMP SYMPOSIA
HOUSTON, TEXAS | SEPTEMBER 9-12, 2019
GEORGE R. BROWN CONVENTION CENTER

MOTOR/GENERATOR SET NON-CONTACTING TORSIONAL VIBRATION MEASUREMENTS

David O'Connor

Engineering Manager
Baker Hughes, A GE Company
Minden, NV, USA

Dr. Lionel Durantay

Chief Technology Leader
GE Power Conversion
Champigneulles, France

Trevor Cowan

Mechanical Engineer
Baker Hughes, A GE Company
Minden, NV, USA

Remy Gerard

Principal Manufacturing Engineer
GE Power Conversion
Champigneulles, France

Brian Howard, PE

Principal Engineer
Baker Hughes, A GE Company
Minden, NV, USA

Lysle Turnbeaugh

Senior Engineer
Baker Hughes, A GE Company
Minden, NV, USA

Olga Malakhova

Senior Analytics Engineer
Baker Hughes, A GE Company
Minden, NV, USA

Emmanuel Goulu

Manufacturing Specialist
GE Power Conversion
Champigneulles, France



David O'Connor is a Principal Engineer and Mechanical Team Lead at BHGE Bently Nevada in Minden, NV. He has developed products for in-core nuclear power reactors, gas and steam turbines, oil and gas exploration, homeland security, power plant monitoring and large rotating machinery mostly focused on researching and developing new transducers and monitors. David received an MScE (Nuclear) and BScE(ChE) from The University of New Brunswick and a BSC(Chemistry) from Mount Allison University



Brian Howard, PE is a Principal Mechanical Engineer at BHGE Bently Nevada in Minden, Nevada. In this role, he focuses on sensor development, diagnostic algorithm development, and research. Prior roles include Signal Processing Engineer and Global Technical Leader for Reciprocating Machinery Diagnostics where he provided diagnostic support to customers to solve problems with rotating and reciprocating machinery. Mr. Howard received a B.S. in Mechanical Engineering from the University of Houston and an M.S. in Electrical Engineering from the University of Washington. He is a member of ASME and IEEE.



Lionel Durantay graduated from the ENSEM (Ecole Nationale Supérieure d'Electricité et de Mécanique) with an engineering degree in 1989 then passed PhD in 1993. He has developed innovative variable speed motors and generators solutions for Oil and Gas and Renewable businesses. He has authored or coauthored 35+ technical papers. He presently holds 12+ patents. He is currently Chief Technology Leader in GE's rotating machines group. lionel.durantay@ge.com



Lysle Turnbeaugh is a Senior Electrical Engineer at BHGE Bently Nevada in Minden, Nevada. Over the last 15 years with Bently Nevada he has worked in product development where he has had the opportunity to develop new sensors, monitoring systems, and IEC 61508 emergency shutdown devices. Mr. Turnbeaugh received a B.S. in Electrical Engineering from the University of Nevada, Reno with recognition from Tau Beta Pi and IEEE-Eta Kappa Nu.



Trevor Cowan is a Mechanical Engineer at BHGE Bently Nevada in Minden, Nevada. In his current role he develops diagnostic analytics. Before working at Bently, he completed GE's Edison Engineering Development Program where he executed four rotational assignments at multiple plants working in quality assurance, research, and product development. Mr. Cowan received a B.S. in Mechanical Engineering from Brigham Young University and an M.S. in Mechanical Engineering from the Georgia Institute of Technology.



Olga Malakhova is a Senior Analytics Engineer at BHGE Bently Nevada in Minden, Nevada. Over the past 16 years she has worked on developing diagnostic algorithms and Decision Support products for Bently Nevada System 1 platform. Prior to that she worked at BRDRC performing research on Pressurized bearings. Ms. Malakhova received her M.S. degree in Mechanical Engineering and Ph.D in Physics and Mathematics from St. Petersburg State Technical University, Russia.



Rémy Gerard graduated from the Université de Lorraine with a University degree in technology (DUT) in 1995 then started to industry as commissioner for AC&DC drives dedicated to metal applications. Later on he took part of large VFD (MV7000 series) prototype developments. He is currently Testing Engineer in Nancy GE's Testbench facility.
Remy.gerard@ge.com



Emmanuel Goulu graduated from Polytech 'Nantes (École polytechnique de l'université de Nantes) with an electrical engineering degree in 2011. He has developed skills in variable speed drive and motors. He is currently test Bench Engineer in GE's rotating machines in Nancy factory (France). Emmanuel.goulu@ge.com

ABSTRACT

Owners and operators of large variable frequency drive (VFD) trains report challenges in detecting and monitoring shaft stress resulting from drive harmonics and inter-harmonic distortion interaction with shaft torsional natural frequencies (TNF's). These stresses are difficult to detect and can lead to failure of the rotor system without advanced warning.

Permanently installed and non-contacting torsional vibration probes provide one method for detecting and monitoring these stresses to allow for advanced warning of failure. Recently, magnetostrictive technology has been applied to large diameter high speed rotating equipment to measure torsional vibration.

Using a test string as an example, the paper develops and presents a torsional vibration model as per API-684. The model describes a fully coupled mechanical-electrical model. Measurements were taken on the train with a variety of measurement systems, including the magnetostrictive sensor, as faults are introduced in the drive system. The model predictions and the measured values were compared including both transient and steady-state data. The paper summarizes recommendations on how to relate measured torsional vibration features to VFD faults and concludes with a discussion of alarm strategies for torsional stress monitoring.

INTRODUCTION

Large variable frequency drive's (VFDs) offer energy savings by controlling the flow of electrical power to match process conditions which lowers the cost of operation [1]. Due to this economic advantage, VFDs find broad application in the oil and gas segments; however, owners and operators of large VFD trains report challenges in detecting and monitoring shaft stress resulting from drive harmonics and inter-harmonic distortion interacting with the shaft torsional natural frequencies (TNF's). These stresses are difficult to detect and can lead to failure of the rotor system without advanced warning [2][3][4][5][6][7][8][9].

Accumulated cycles of stress reduce the remaining life of the shaft. While all shafts are designed to carry stress in the form of torque, undetected large oscillations in torque can result in premature fatigue related failures. To better understand how to measure torsional vibrations in practice, a model was developed to describe the interactions between the VFD, the motor electromagnetic circuit, and the rotor string torsional response. In addition, results of torsional measurements on a VFD test bed are provided and compared to the model used to predict torsional vibration amplitudes and frequencies. The conclusion of the paper includes recommendations for alarm strategies.

TEST SYSTEM OVERVIEW

Figure 1 shows the equipment and instrumentation used for development in this paper. The instrumentation included voltage and current monitoring of the line-in power, proximity probe monitoring of the bearing closest to the magnetostrictive torsional vibration sensors, the magnetostrictive torsional vibration sensors, and an in-line reference torsional vibration sensor. Figure 2 shows the orientation angles and installation photos.

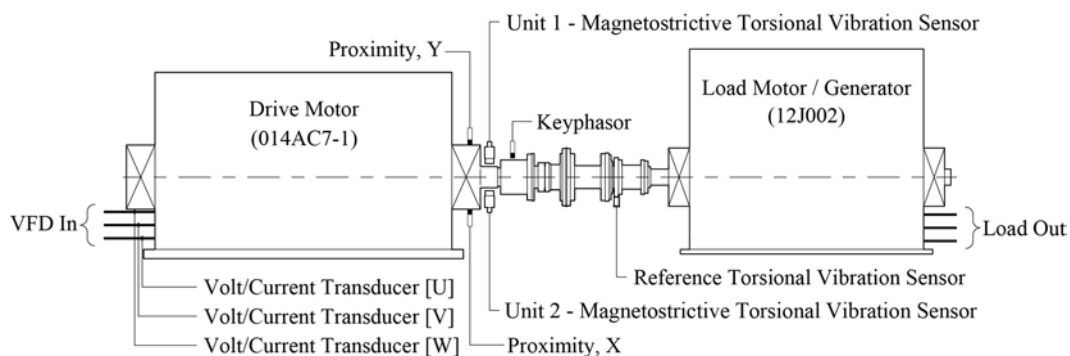


Figure 1 - Test Equipment Arrangement

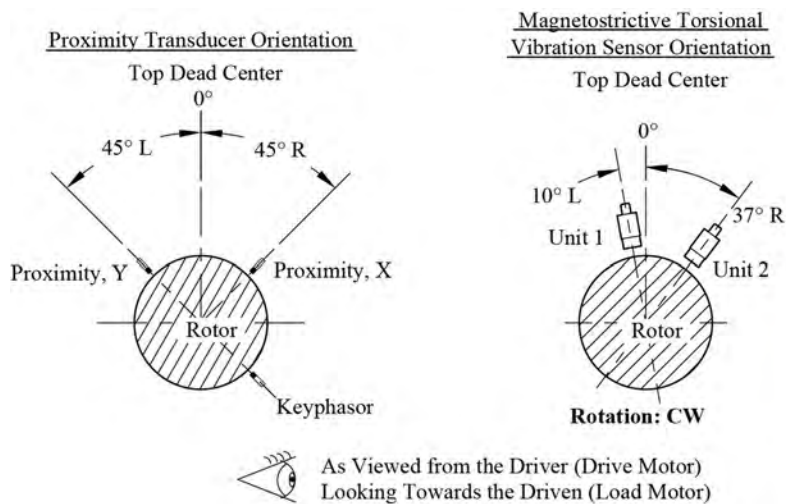


Figure 2 - Probe Orientation Angles (Left) and Installation Photo (Right)

The test string consisted of a VFD, an induction drive motor, coupling, torque limiter, and an induction load motor (generator). Table 1 describes each component in detail and Figure 3 shows pictures of the equipment used in the test.

Table 1 - Description of Test Equipment

Component	Description
Drive Motor (014AC7-1)	Number poles: 2 (1-pair) Nominal power: 5350 kW [7174 hp] Synchronous speed: 3000 RPM Nominal Voltage: 6000 V Nominal Current: 606 A Nominal Frequency: 50 Hz
Coupling	Rigid
Torque Limiter	Minimal clutch torque: 7500 N-m [5532 ft-lb] Maximum clutch torque: 15000 N-m [11064 ft-lb]
Load Motor (12J002)	Number poles: 4 (2-pair) Nominal power: 4825 kW [6470 hp] Synchronous speed: 1516 RPM Nominal Voltage: 4000 V Nominal Current: 802 A Nominal Frequency: 50 Hz



Figure 3 - Test String Arrangement

POWER SYSTEM DESCRIPTION

This section describes the transfer function for the combination of the power system and the motor simulation. This section provides an overview of the topologies and operating characteristics of the one used in this test; many references describe large VFD design and operation in detail [10][11]. Appendix A includes the derivations and model for this VFD.

VFD systems convert fixed frequency AC power to a variable frequency AC power suitable for the motor drive by converting the incoming fixed frequency AC power to DC power and then back to variable frequency AC power for the motor. There are three drive and motor configurations [13][14]:

- Load Commutated Inverter (LCI) and synchronous motor. The inverter thyristors require some reactive power to commute so LCI controller adjusts the motor Power Factor (PF) to 0.9 leading for this switch-off commutation.
- Voltage Source Inverter (VSI) via Pulse Width Modulation (PWM) and synchronous motor adjusting PF around one.
- VSI (PWM) and induction motor at requested PF maximizing the torque generation.

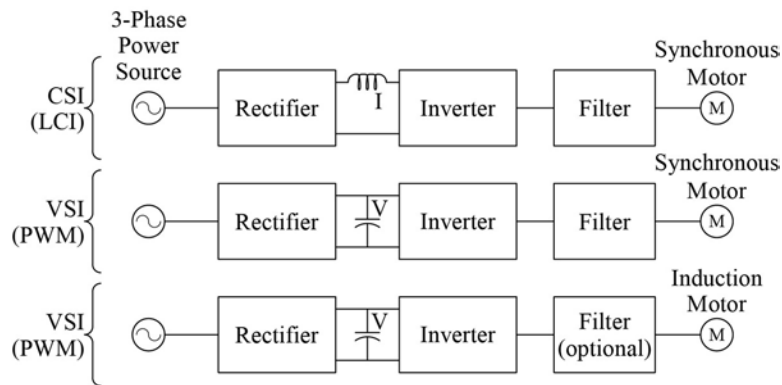


Figure 4 – VFD topologies

The test string in this paper uses a VSI topology in a back-to-back test configuration. The high-power VSI PWM drive is available in a 3-level topology with the neutral point clamped by diodes. With such a topology, and the increasing capacity of the power devices, a VSI composed of a single power device per arm can deliver around 15 MVA with an output voltage of 3.3 to 3.6 kV. Specially packaged insulated-gate bipolar transistors, Press Pack Injection-Enhanced Gate Transistor (IEGT), are at the heart of the inverter-to-rectifier bridge design providing switching for both the rectifier and inverter side of the drive.

The supplying grid connects to the front-end rectifier side of a VSI and produces the pseudo constant DC voltage that will be chopped by the inverter to deliver the desired voltage and frequency to the motor. There are two main types of front ends: Diode Front End (DFE) and Active Front End (AFE). The DFE is composed of one or more diode bridges, usually connected in series. As the current cannot be reversed in the diodes, its usage is restricted to drives that do not require power regeneration from the motor to the grid.

The AFE is composed of self-commutated power devices. Usually, its components and its topology are the same as the ones used for the inverter to which it is associated thus making the AFE rectifier a mirrored image of the inverter. The AFE regenerates power from the motor to the grid; regeneration is necessary for the machine used in generator mode in a back-to-back arrangement. In addition to the drive itself other components may include input transformer and output filters on the motor side.

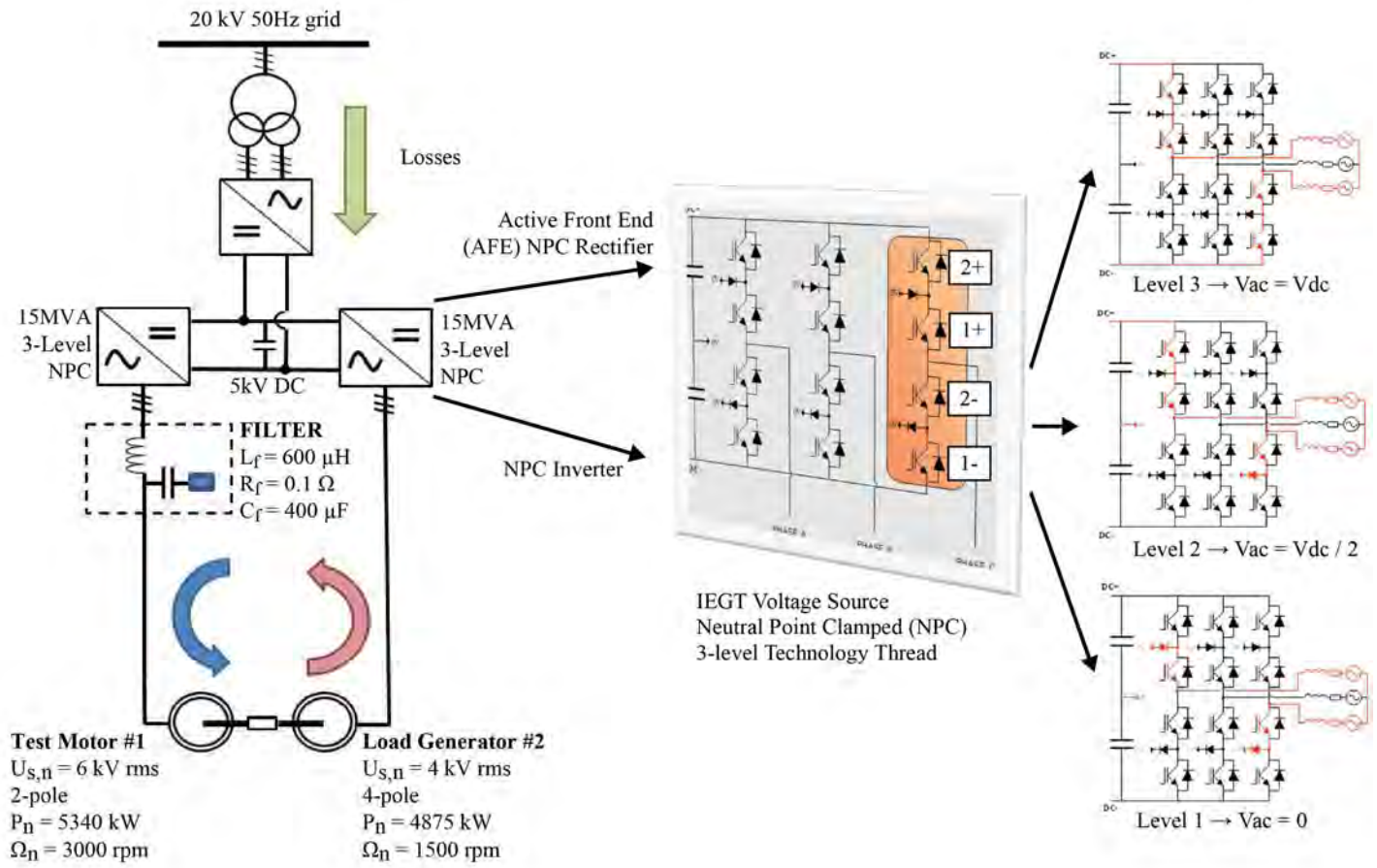


Figure 5 - Induction motors and VSI back-to-back test configuration

The decoupling between the rectifier and the inverter is much higher in a VSI than in an LCI topology. The increased decoupling results from larger DC energy storage in the VSI DC capacitors, compared to the energy stored in the LCI DC reactors. For this reason, VSIs do not produce significant inter-harmonics, especially with AFE rectifiers. The VSI generates voltage harmonics, V_h , to the motor, in contrast to an LCI that generates current harmonics, I_h , to the motor. For the VSI system, the higher the motor impedance, Z_h , the lower the harmonic currents, $I_h = V_h/Z_h$. For this reason, VSI systems, with high PWM frequencies, tend to be a lower source of torsional pulsation. Appendix A explains this in more detail.

Each component modifies or creates a dynamic power signal with the desired frequency, shown schematically in Figure 6. The power signatures of each section contribute to the torsional vibration forcing function in the motor itself. The primary frequencies of interest are the line-in frequency, f_{in} , and line-out frequency, f_{out} .

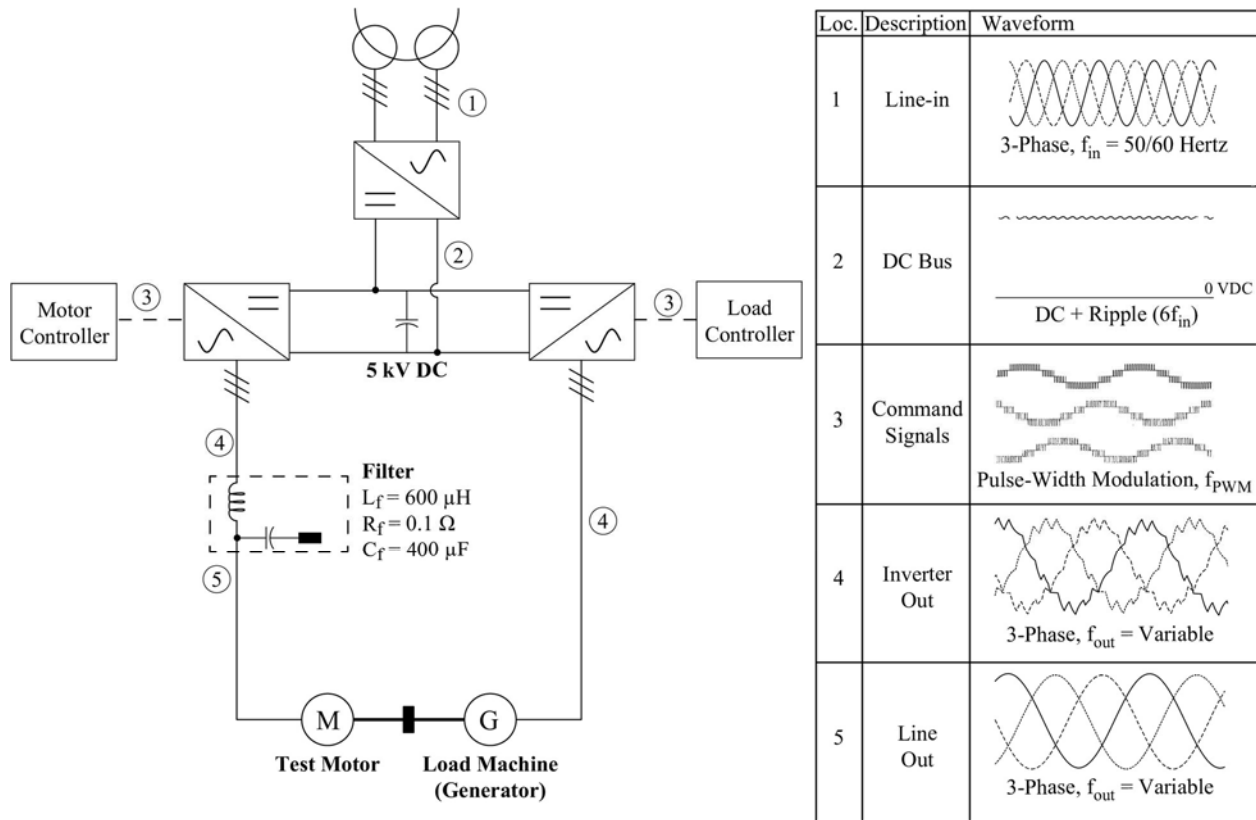


Figure 6 – VFD System Operation

It is important to understand the excitation features of the electrical power signatures because they interact with the motor and rotor string. Non-sinusoidal components in the VFD result in current harmonics. Appendix A provides an overview of the motor equivalent circuit and explains how voltage and current relate to the air-gap torque (torsional vibration forcing function) for this motor. The current applied to the motor field is 3-phase so frequencies of interest for current are different than those of torsional frequencies. This train had current transducers for the drive motor. Table 2 provides a reference for common harmonics found in motor currents.

Table 2 - Motor current harmonics.

Description	Source	Frequencies
Characteristic integer harmonic currents	Current has non-sinusoidal components. A symmetrical 3-phase machine should produce no harmonics divisible by 3 [12]. The $n * p_M - 1$ will rotate opposite fundamental and $n * p_M + 1$ will rotate with the fundamental.	$f_{char(i)} = (n * p_M \pm 1) * f_{out}$ Where: n Integer: 1, 2, 3, ... p_M Pulse number of inverter f_{out} Motor electrical frequency
Characteristic inter-harmonic currents	The inverter is not perfectly isolated from the rectifier and some DC ripple appears on the output. [11] and [15].	$f_{char(n)} = (n * p_S \pm 1) * f_{in} \pm m * p_M * f_{out}$ Where: n, m Integer: 1, 2, 3, ... p_S Pulse number of rectifier f_{in} Line-in frequency p_M Pulse number of inverter f_{out} Motor electrical frequency

Current passes through the induction motor stator and generates a magnetic field that couples to the motor rotor. This field induces currents, which in turn, produce a magnetic field that reacts to the stator magnetic field. The interaction between these two fields generates torque. If the induction motor rotor turns at the same frequency as the stator EM field, then no torque is produced. As the rotor speed decreases with respect to the stator electric frequency (“slip”) torque is produced. Variation in the current and interaction across harmonics, produce variation in the torque (torsional vibration). Table 3 summarizes the common torsional vibration frequencies. Appendix A provides more details on the motor-VFD interactions and the current to torsional vibration interactions.

Table 3 – Motor torsional vibration harmonics

Description	Source	Frequencies
Characteristic integer harmonic currents	Torsional pulsations arise from interaction of current harmonics with rotating field [11], [15] and [17].	$f_{char(n)} = n * p_M * f_{out}$ Where: n Integer: 1, 2, 3, ... p_M Pulse number of inverter f_{out} Motor electrical frequency
Characteristic inter-harmonic currents	The energy storage within the DC link is finite which allows some ripple. Incomplete isolation between the inverter and rectifier section pass the ripple into the inverter which results in interference from the line-in frequency, f_{in} , and line out frequency, f_{out} [11].	$f_{non(n,m)} = n * p_M * f_{out} \pm m * p_s * f_{in} $ Where: n, m Integer: 1, 2, 3, ... p_M Pulse number of inverter f_{out} Motor electrical frequency p_s Pulse number of rectifier f_{in} Line-in electrical frequency

MECHANICAL SYSTEM DESCRIPTION

The mechanical system consists of an induction drive motor rigidly coupled to a reference torsional vibration transducer and mechanical torque limiter driving an induction load motor, shown in Figure 7. As described in [17] station numbers were assigned to the rotor and a mass elastic system was developed.

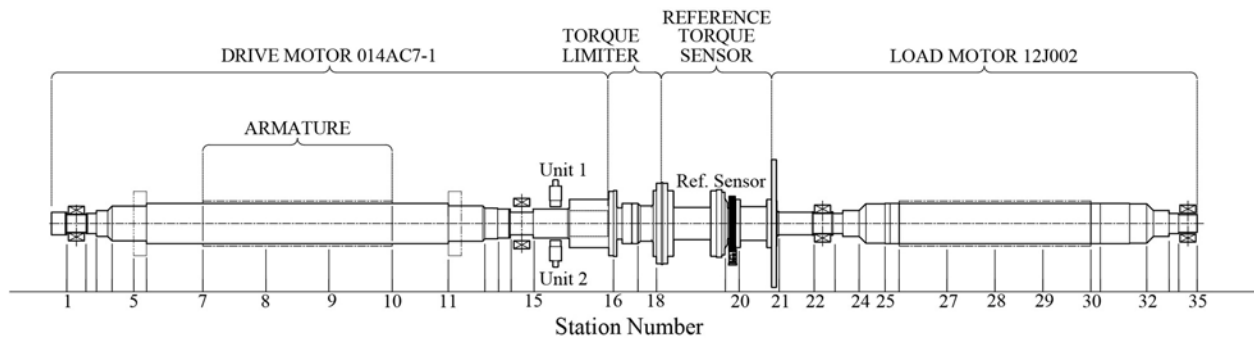


Figure 7 - Test rotor string.

The mechanical system response is derived using a lumped parameter model approach described in Appendix C. The load motor and drive motor field were broken into multiple station numbers to improve model accuracy. Figure 8 shows the lumped parameter schematic. The lower stiffness and the larger inertia values due to the 4-pole construction in the load motor field result in higher amplitudes compared to the rest of the string; therefore, the load motor field has nodal points in one or more of the lower torsional modes.

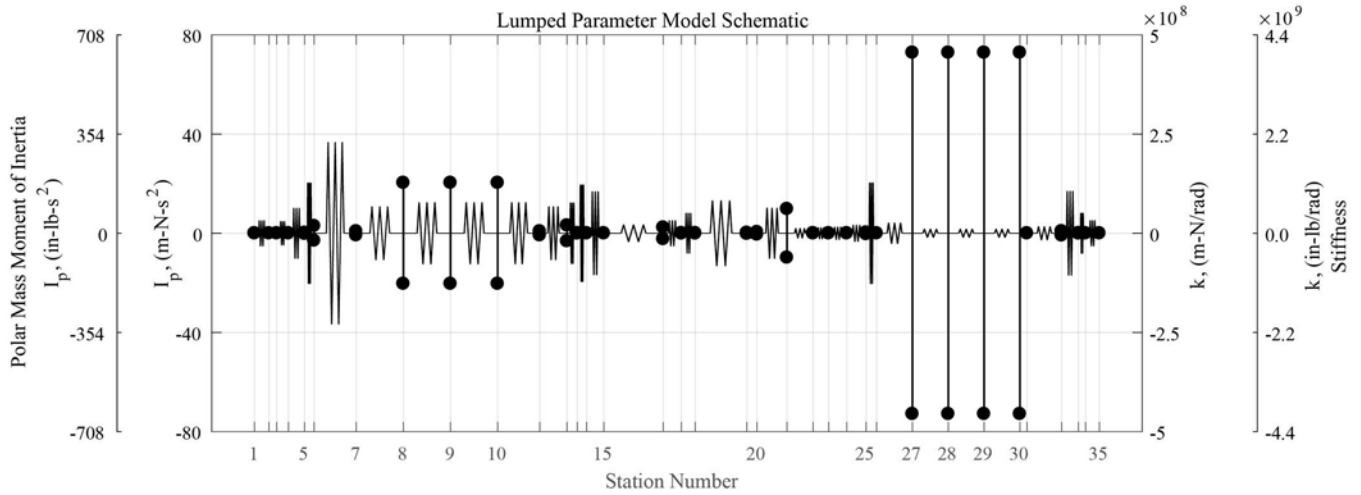


Figure 8 – Lumped parameter model diagram.

Figure 9 shows the mode shapes for the test stand. As expected from the lumped parameter model two higher modes are load motor modes. Only the lower mode has a nodal point between the machine cases. The reference torsional vibration sensor has been designed to be compliant (low stiffness) which gives the steep slope to the mode shape at station 20. The magnetostrictive torsional vibration sensors, located between stations 15 and 16, view a part of the mode shape with little deflection. This implies a stiff section with less stress reaction to input torques, compared to the section with the reference torsional vibration sensor.

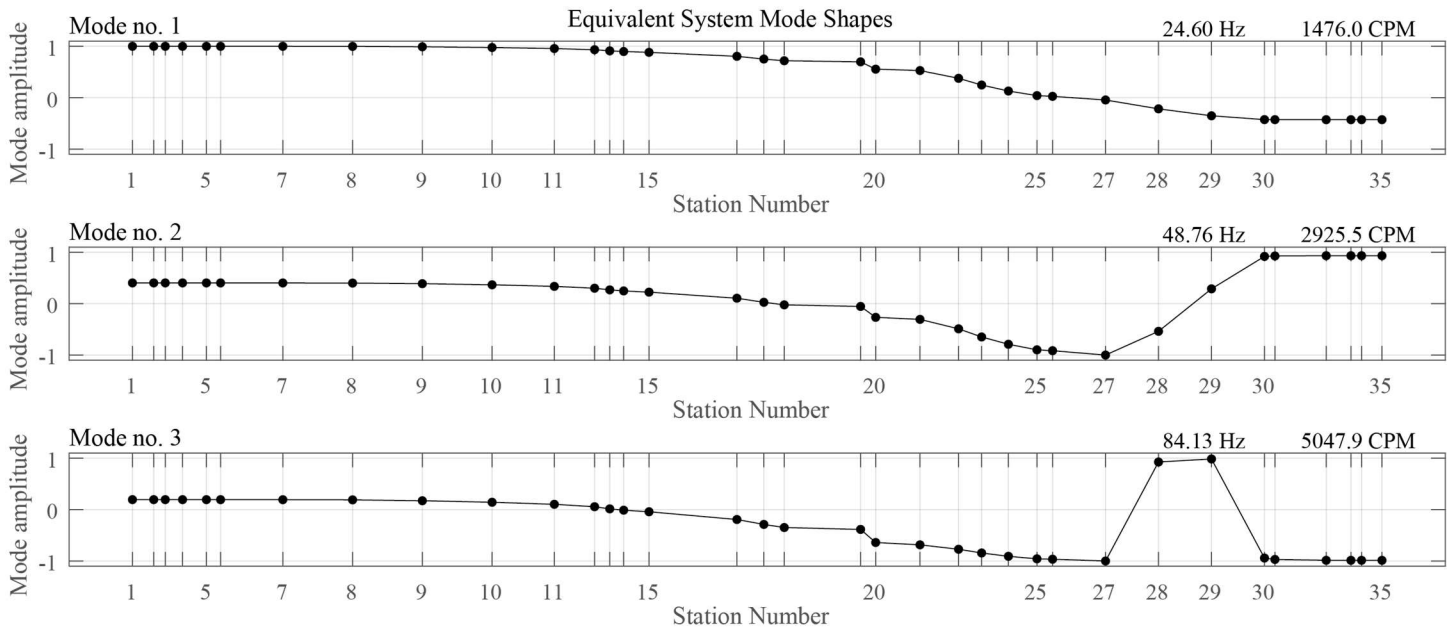


Figure 9 – First three torsional mode shapes

ESTIMATED RESPONSE AT MEASUREMENT PLANES

The response at the measurement planes due to torsional forces in either the driver or load motor can be estimated by including damping and calculating the forced torsional response. Figure 10 shows the response at the reference torsional vibration sensor and Figure 11 shows the response at the magnetostrictive torsional vibration sensors to an impulse at the drive motor.

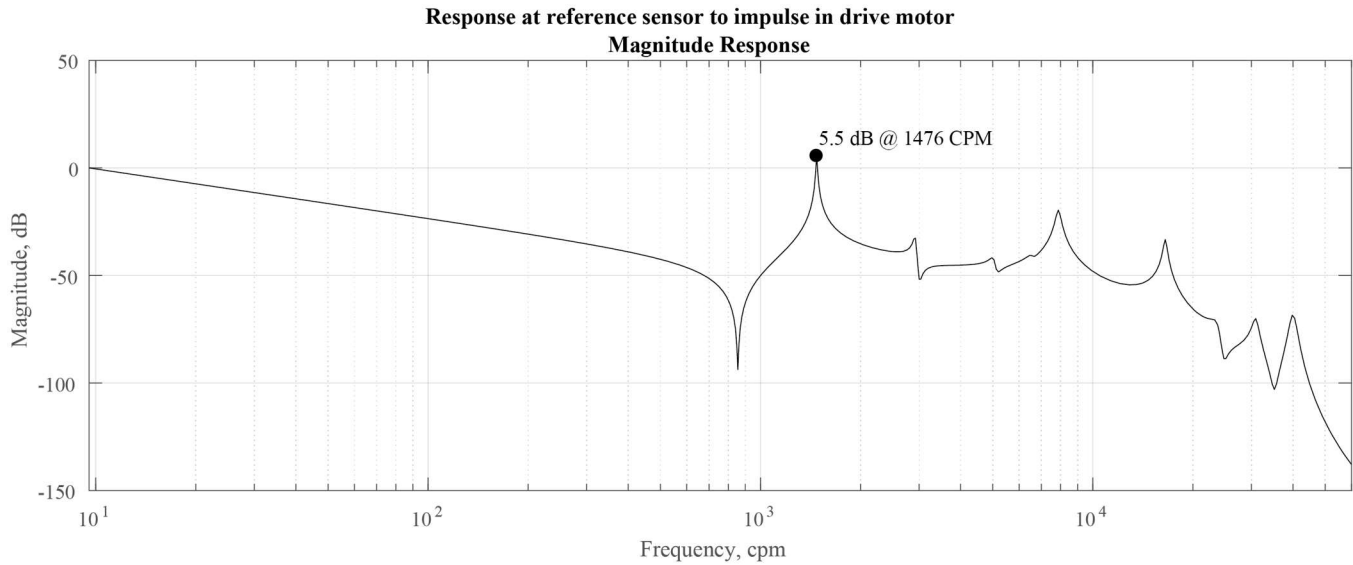


Figure 10 – Estimated response at reference torsional vibration sensor plane to impulse in drive motor field.

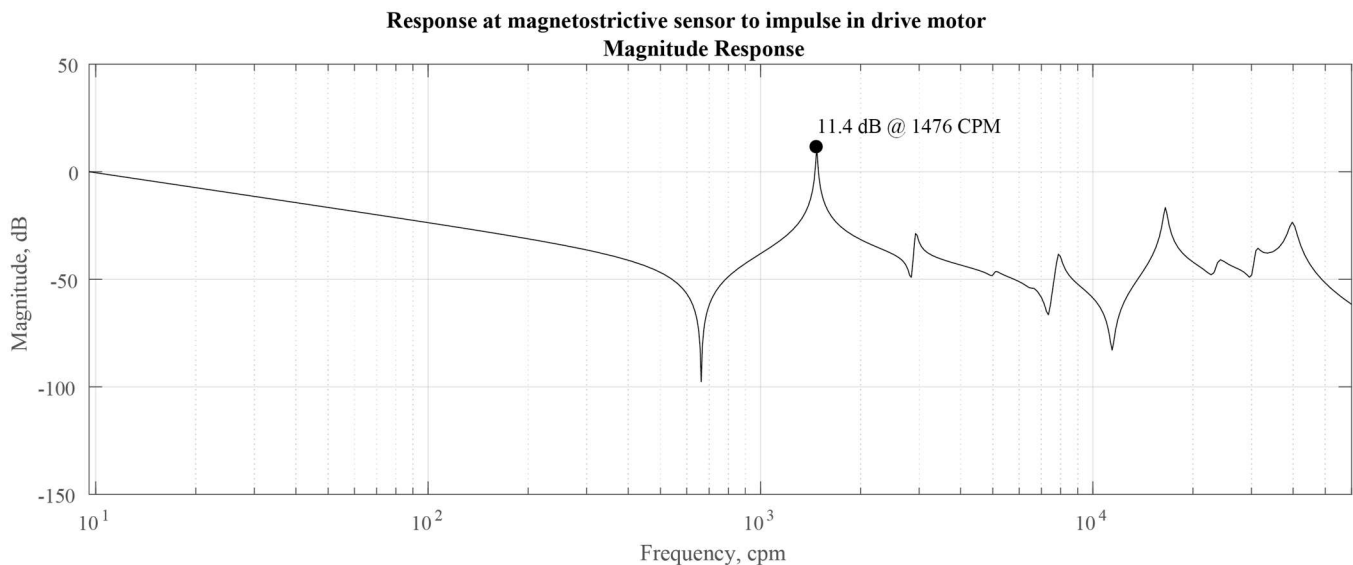


Figure 11 – Estimated response at magnetostrictive torsional vibration sensor plane to impulse in drive motor field.

The model included internal damping calculated as described in Appendix C but no external damping. Both the reference and magnetostrictive torsional vibration sensors should have a good response to the first torsional resonance when looking at the torque values. Responses for the other resonances will be diminished because the rotor string acts like a low pass filter because it is difficult to physically move large masses like the rotors at high frequencies. For this reason, even if high frequency torsional forcing functions exist in the air-gap torque they tend to have a small effect on the shaft string itself. Except if those frequencies fall on a low order TNF or harmonic of a low order TNF.

CAMPBELL DIAGRAM

Combining the electric forcing functions from the VFD, described in Table 3, with the mechanical system allows for the Campbell diagrams to be generated. Following the styles of [17] and [19], Figure 12 shows the frequency map for the integer harmonics (first row of Table 3) and Figure 13 shows the frequency map for the inter-harmonics (second row of Table 3). The wide range of operating speeds on this test stand have several intersections for the inter-harmonic components. Figure 13 lists all the interface regions; however, the combination of the motor field attenuation (Appendix A) and low-pass filter effect of shaft string result in attenuated response to higher frequency components (above ~1000 CPM). Components below this region need to be carefully monitored due to the possibility of higher torsional stresses. Figure 12 highlights one of these areas of interest with an arrow.

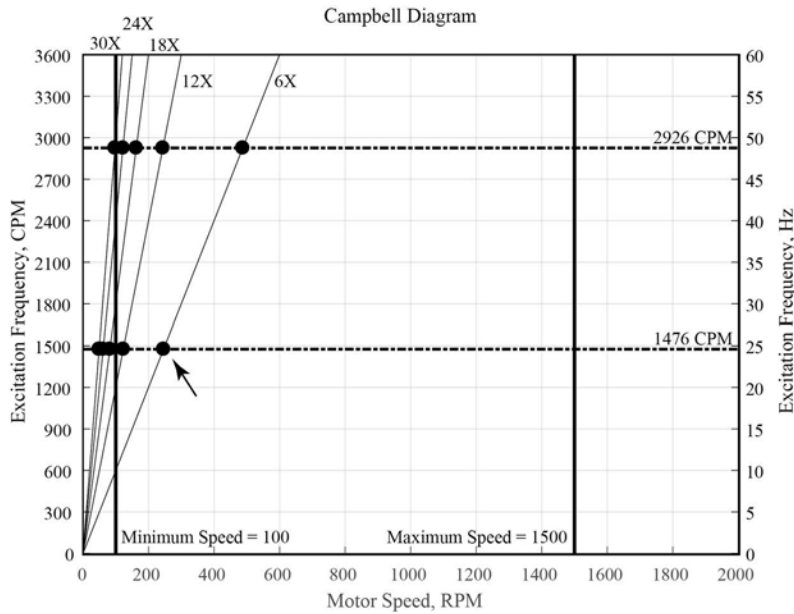


Figure 12 - Campbell diagrams (frequency map) for integer harmonics.

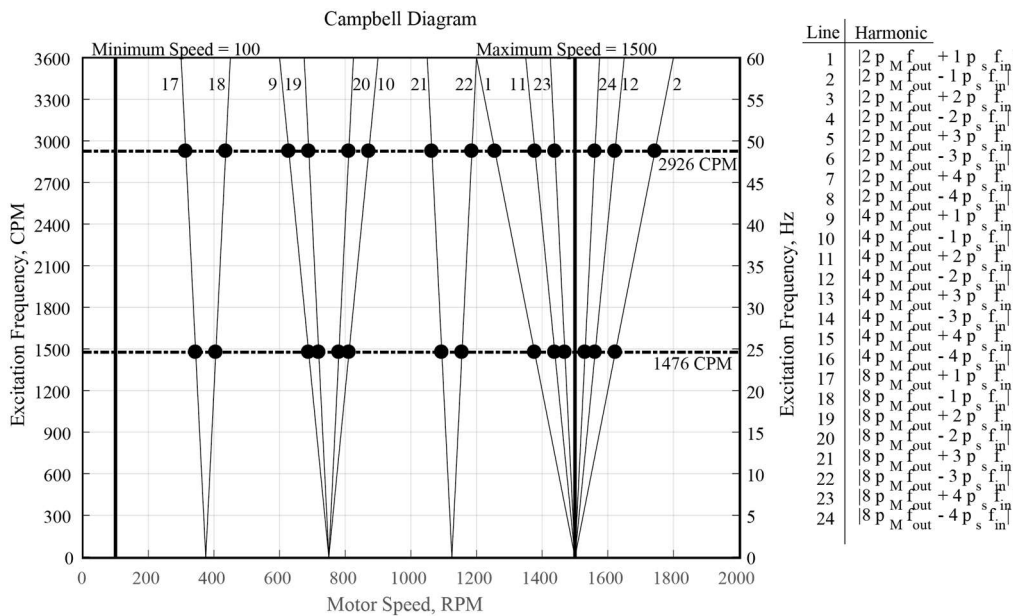


Figure 13 - Campbell diagrams (frequency map) for inter-harmonics.

DATA ANALYSIS

Lateral and torsional data were taken on the test stand. Machines tend to be much better instrumented for lateral vibration monitoring and in some cases, there can be important cross-coupling effects between torsional and lateral vibration modes. Prior to examining the torsional data, the lateral behavior of the machine was reviewed.

The lateral model for the machines predicted the first balance resonance would be near 2100 RPM. The machine operated at 1500 RPM, well below this first resonance. The filtered 1X bode plot, shown on left side of Figure 14, does not indicate a resonant response which is the expected behavior. The amplitudes are very low from 200 to 850 RPM, so the phase calculation has some uncertainty in it. Otherwise, the phase is flat. The filtered 2X bode plot, shown on the right side of Figure 14, shows a phase change and two peaks at slightly different values, 912 RPM for the vertical probe and 922 RPM for the horizontal probe. This 2X indicates a lateral resonance near twice the values at about 1830 RPM. This is lower than the lateral model predicted and is likely due to the addition of brake disc (additional mass) and torque limiter (compliant coupling) that brought the lateral resonance down.

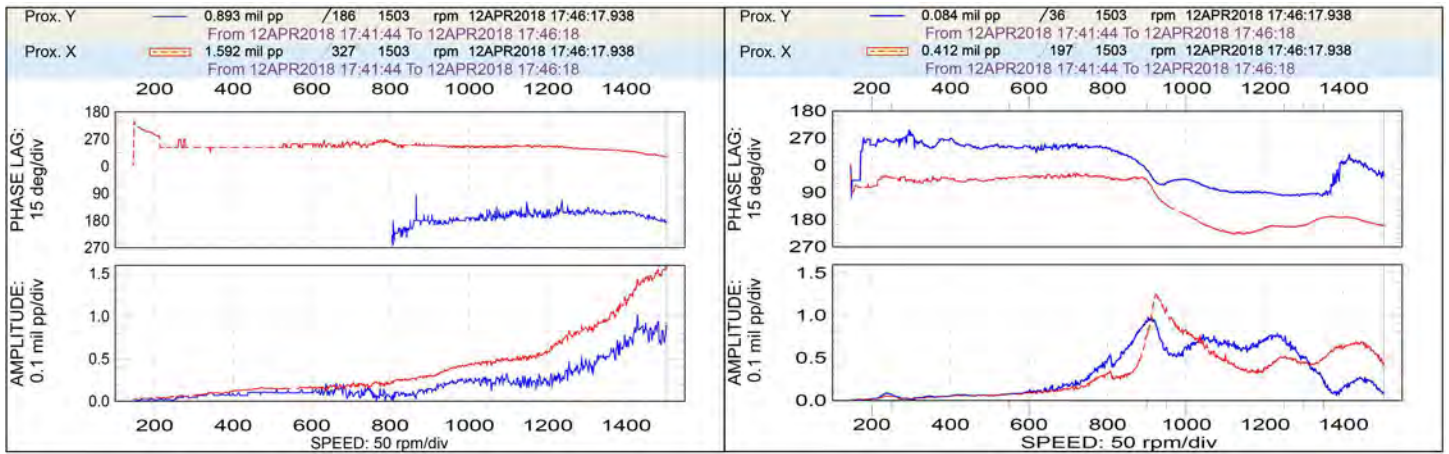


Figure 14 - Filtered 1X bode plot (compensated) in the left pane and filtered 2X bode plot (compensated) on the right pane. Data during startup.

The orbits at the bearing closest to the magnetostrictive sensors, shown in Figure 15, are forward processed (blank-to-bright is in the same direction as rotation) and the shape is elliptical. The major axis is declined and nearly horizontal in the direct orbit. This is likely due to the weight of the rotor of the drive motor which is slightly distorting the orbit. As would be expected for an orbit of this shape, the 1X orbit is also inclined horizontally and is forward processed. The bode and orbit plots show that the rotor system is operating as expected, except for the lower value for lateral resonance.

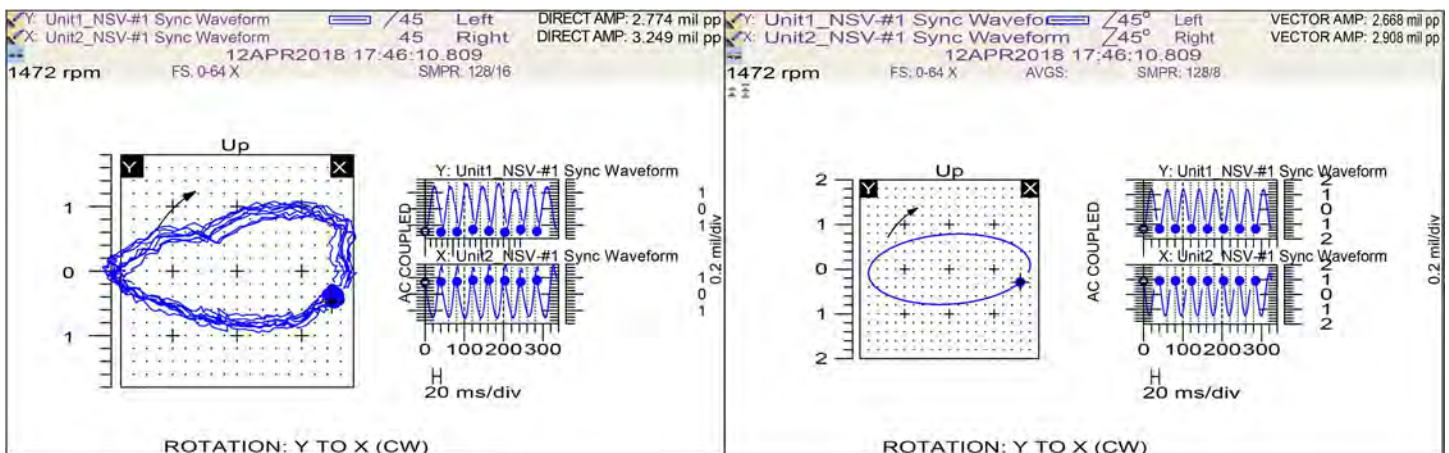


Figure 15 - Direct and filtered 1X orbit at full speed.

The drive motor can be brought up to speed slowly allowing the torsional response to the shifting VFD frequencies to be measured. Figure 16 shows the system response as speed increases and focused on the areas of torsional resonance. The top pane shows the rotor speed as a solid line and the drive motor electrical frequency as a dashed line. The middle plot shows the slip frequency where slip is the difference between the rotor speed and drive motor electrical frequency in percent. The bottom plot shows the torsional vibration from the reference sensor.

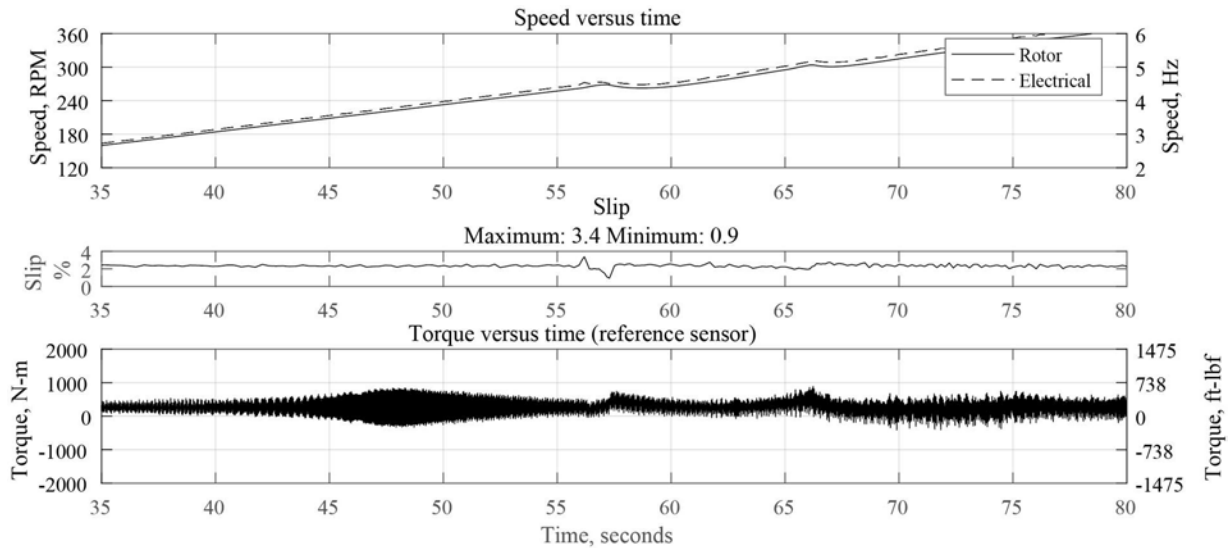


Figure 16 – System torsional response as speed increases.

From the Campbell diagram in Figure 12 the 6X should excite the torsional resonance at 246 RPM (this is the point highlighted by the arrow). The motor reaches 246 RPM at about 52 seconds on the x-axis in the plots of Figure 16. This resonant response can be seen in the reference sensor signal peaking at about 48 seconds or 226 RPM. This response is caused by the 6X frequency exciting the first TNF near 22.5 Hz [1,356 CPM], which is slightly below the predicted value of 24.6 Hz [1476 CPM].

Once the system reaches steady-state, the load motor begins to apply torque to the system. Figure 17 shows system response as load increases. This plot includes the same measurements as before but adds the signal from magnetostrictive torsional vibration sensors. As expected for an increase in load, the slip frequency increases and both the reference and magnetostrictive sensors show an increase in torsional vibration. To understand the dynamics in these signals it is helpful to look at the signals in more detail.

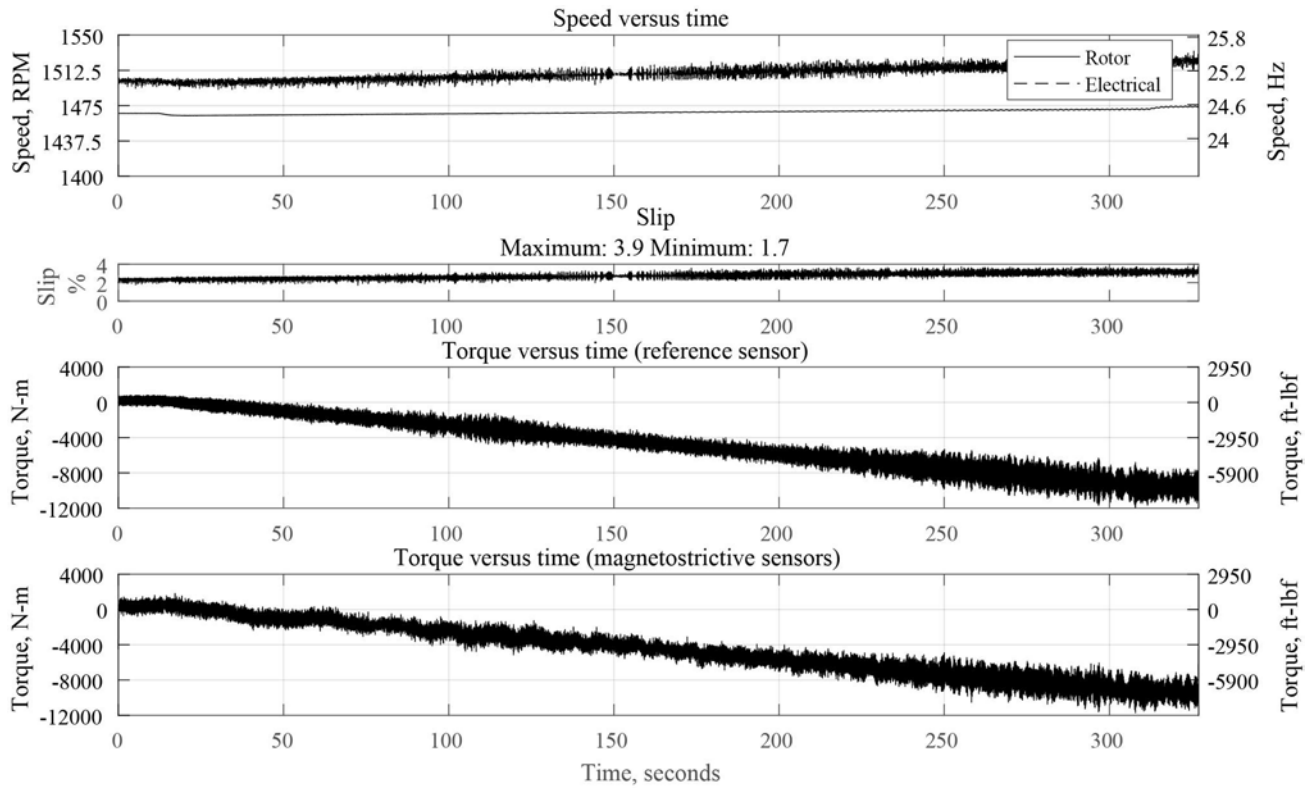


Figure 17 - System torsional response as load increases.

Figure 18 shows the steady-state response as the train reached full load. In this format the periodicity of the torsional vibration can be seen in both the reference and magnetostrictive torsional vibration sensors. The peaks are separated by about 0.03 seconds for a frequency of about 33 Hz. This frequency does not correlate with the TNF identified earlier or any of the forcing frequencies from Figure 12.

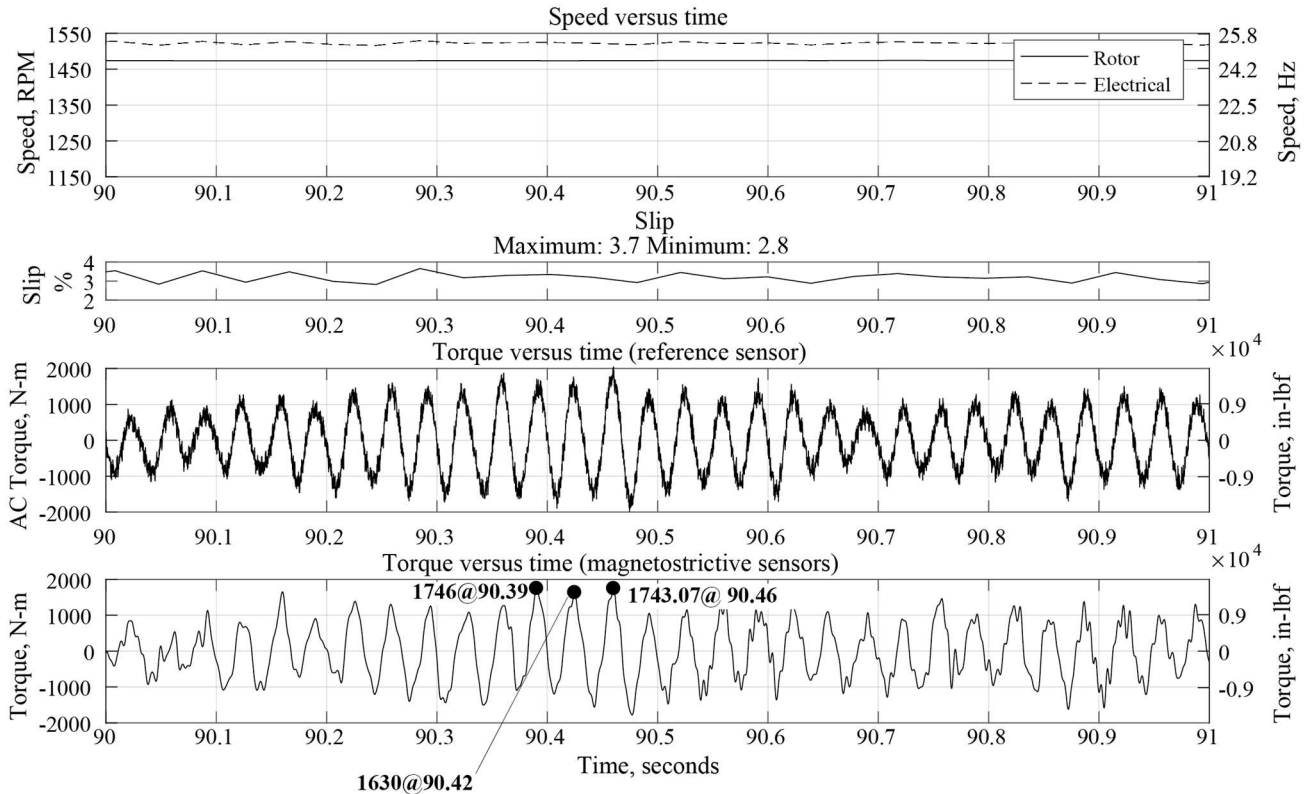


Figure 18 – System torsional response at steady-state conditions.

This frequency persists throughout the measurement; however, the amplitude changes show, for steady-state drive motor field frequency and shaft RPM, a modulation in the time domain of both systems. A frequency domain analysis will be done next to more precisely identify the frequency.

The system response in the frequency domain, shown in Figure 19, has a clear peak in both system at 30.00 Hz [1800 CPM] with an amplitude of 818 N-m [7239 in-lbf]. Referring to Figure 17 where the load reaches about 10,000 N-m, this response represents nearly 10% of full load torque.

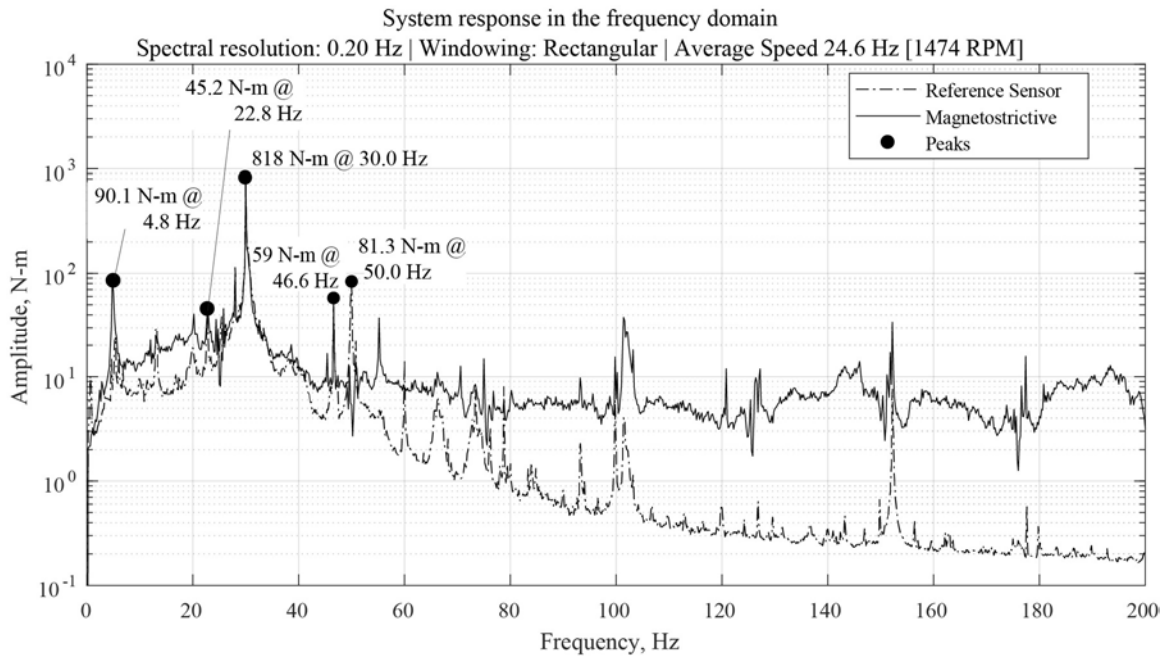


Figure 19 - System torsional response in the frequency domain.

If the first mode fundamental were to be excited, based on the model and the start-up data, that response should fall in the range of 22.6 Hz [1356 CPM] to 24.6 Hz [1476 CPM]. Both systems do show peaks at 22.8 Hz [1368 CPM] and 46.6 Hz [2796 CPM] which are likely the first TNF and second TNF responses, respectively, due to background excitation. As anticipated from the transient analysis the measured TNF's fall below those predicted by the model.

VFD systems are often cited as the source of torsional excitation; however, the response of 30.0 Hz [1800 CPM] in Figure 19 does not match the expected frequencies of excitation. To further validate that the applied torsional force is not the cause of the response, Appendix A introduces a helpful method that used the estimated instantaneous power in the rotor, derived from the motor stator currents and voltages shown in Figure 20, to calculate the torsional force acting on the motor field. This method was applied to the full load data to estimate the frequency domain forcing function from the drive motor air-gap torque.

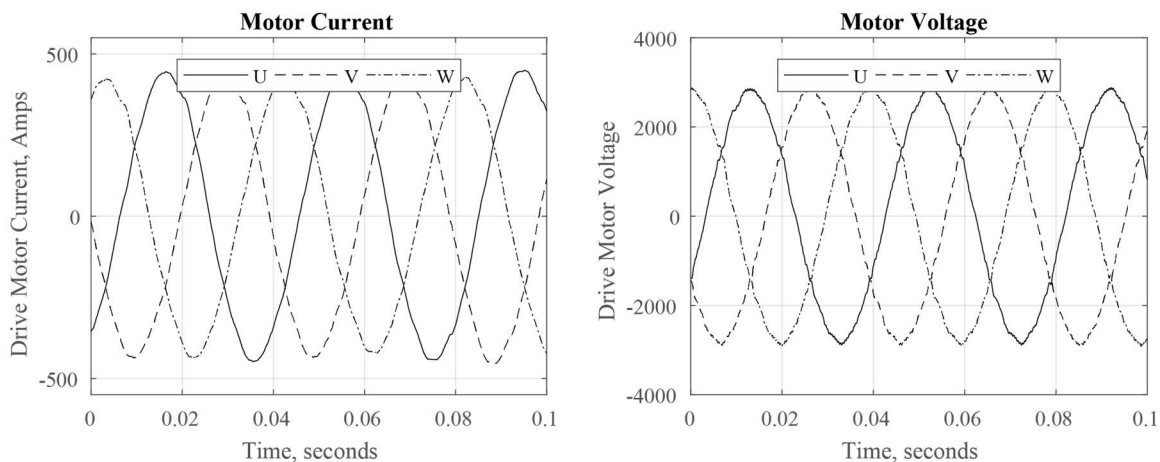


Figure 20 - Drive motor and current signals at nominal speed of 1500 RPM.

Figure 21 shows the air-gap torque in the frequency domain. It has few components below 200 Hz so the horizontal axis in Figure 21 is much wider than that of Figure 19 to show the larger components. The model is straightforward yet provides a detailed perspective on the air-gap torsional forcing function. Most of the forcing functions are at 800 Hz or higher which are damped by the mass of the rotor and do not have a large effect on the torsional response as is characteristic of PWM drives. There is a 50 Hz component in the air-gap torque that also appears on both the reference and magnetostrictive torsional vibration sensors; however, no significant excitation falls near 30 Hz.

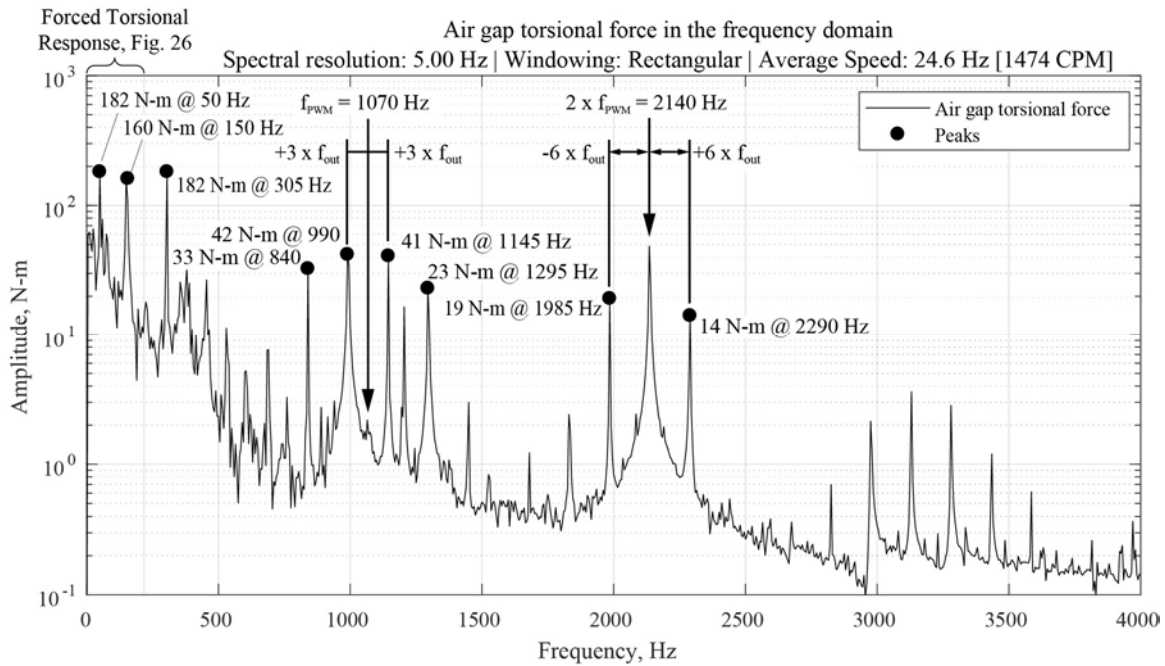


Figure 21 - Estimated drive motor air-gap torque spectra.

The 30 Hz response does not seem to have originated from the VFD; a cross-coupling mechanism between the lateral resonance into the torsional system could be the cause, especially since the 1800 CPM torsional response is so close to 1830 CPM lateral resonance. Lateral vibration can be a cause of cross-coupling because the shaft deflection shifts the rotating masses from the centerline [26] [27]. Figure 22 shows a straight rotor operating without deflection on the left and one operating with deflection on the right. In the case of lateral vibration, the disk center has shifted from the shaft centerline and the disk center now processes about the shaft centerline, at distance r . Since the disk operates at a different position, the polar moment of inertia has changed causing a periodic torque to appear in the shaft string. Figure 19 shows the torsional vibration values are 38 N-m and 22 N-m for the 1X and 2X components respectively; therefore, they are not a factor in the 30 Hz component.

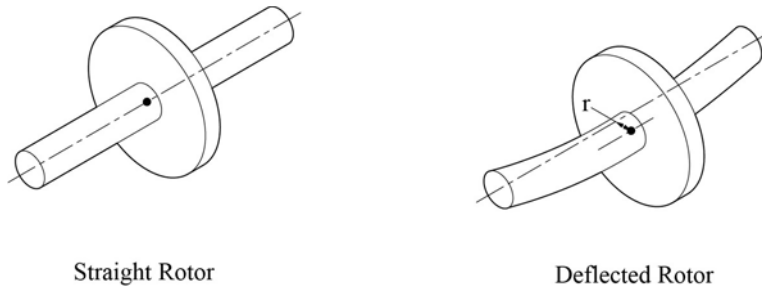


Figure 22 – Illustration of rotor deflection

Cross-coupling can also be caused by shaft anisotropy in the presence of preloads [26]. The drive and load motor fields have anisotropy and operate under a gravitational preload. The anisotropy comes from the geometry of the field, shown in outline in Figure 23 for the load motor (largest mass and most compliant field). When the rotor angular position matches the left orientation there is more resistance to the gravitational load than when in the position on the right. Each time the rotor changes from the position on the left to the position on the right there is a “snapping” effect resulting in torsional excitation. This occurs each time a web moves into the vertical position, or 6X per revolution. At the operating speed of 24.6 Hz [1474 CPM] this 6X is well above 30 Hz. This is a minor component in Figure 19, less than 1 N-m in amplitude.

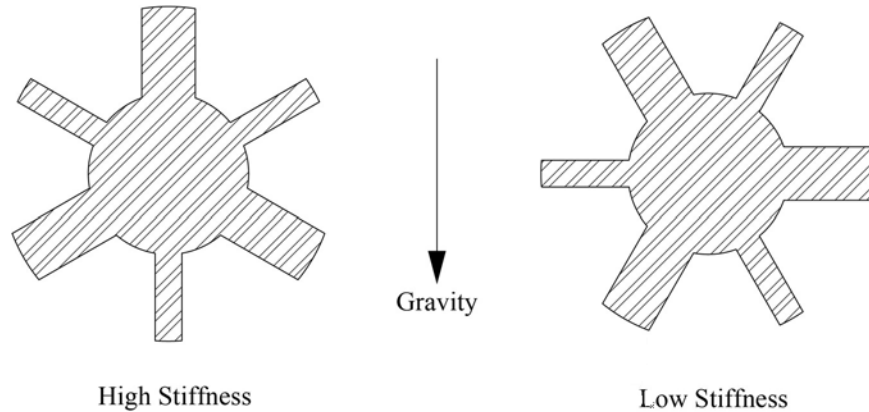


Figure 23 - Load motor field cross-section schematic

Ruling out direct VFD excitation and cross-coupling leaves few candidates. The most likely candidate seems to be electro-motive (EM) force connecting the rotor string to ground as discussed in [7]. Using the estimation methods suggested in [7] with the rotor anisotropy acting as the forcing function for torsional vibration, the degenerate mode frequency is predicted to be 3.8 Hz, which is close to the 4.8 Hz observed in Figure 19. The predicted second mode is 25.1 Hz, which is lower than the 30 Hz observed in Figure 19. Following the suggestion in [7] and using the measured data to tune the model results in values of 4.8 Hz and 26.8 Hz for these two modes. Considering the uncertainty in field stiffness and damping values over temperatures, this is reasonable agreement between the model and measured data.

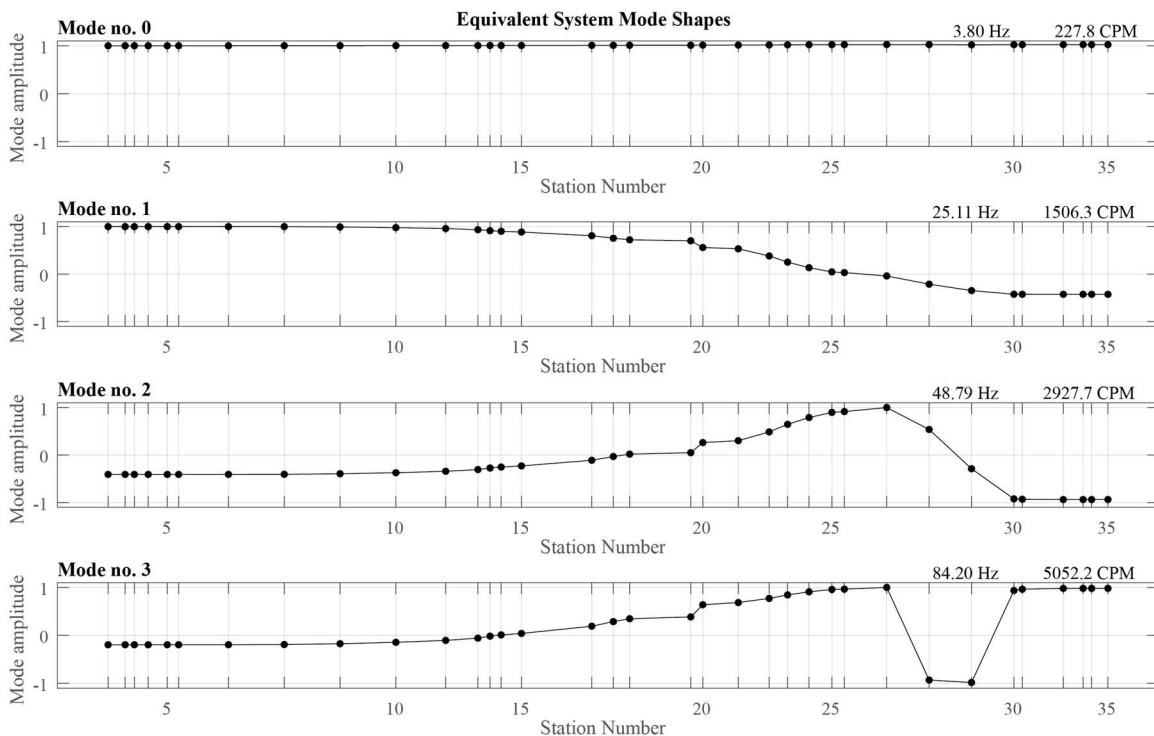


Figure 24 - Torsional mode shapes with EM stiffness to ground.

ALARM STRATEGIES

Using the air-gap torque along with the motor equivalent circuit, described in Appendix A, and the system torsional response to determine probable fault frequencies was valuable. As noted in Appendix A and the discussion around the torsional model, alarming and torsional vibration detection should focus from DC to 500 hertz because motor windings and rotor masses dampen torsional forces higher than this. While many sources discuss the need to monitor excitation frequencies associated with various VFD systems, for example Table 3, few discuss the need to monitor cross-coupling effects on shafts, especially those with anisotropy.

Alarm configurations on systems with anisotropic rotors should include frequency bands around the sub-harmonic, harmonic, and super-harmonic locations for lateral resonances. Additional case histories from these alarms will be useful in determining which of these bands should be monitored more closely, possibly even for shutdown.

Steady-state operation, shown in Figure 18, has some torque pulsations which should be monitored. The internal design criteria used by the manufacturer considers the maximum air-gap torque pulsation value in the time domain signal to be $\pm 12\%$ of the air-gap rated torque. The $\pm 12\%$ value corresponds to a fluctuating unidirectional stress ratio of fatigue, $R = (1-0.12) / (1+0.12) = 0.88 / 1.12 = 0.78$, which is conservative for commonly used shaft materials. For the 2-pole motor in this paper, the rated torque is $(5350 \text{ kW}) / (2 * \pi * 50 \text{ Hz}) = 17030 \text{ N-m}$. Using the $\pm 12\%$ criteria, the maximum torque modulation is $\pm 2043 \text{ N-m}$ on the time signal which is greater than the pulsations shown in Figure 18.

As torsional vibration monitoring matures, alarming strategies will also need to relate the measured torsional vibration to stress in the shaft as discussed in Appendix D. Alarms will need to consider the combination of static and dynamic stresses. Such monitoring could include detection of cycles that would then be classified, based on amplitude, as either low-cycle or high-cycle events and counted to estimate the remaining shaft life.

CONCLUSIONS

This paper demonstrated a method for estimating the air-gap torque in an induction motor and showed how magnetostrictive sensors can be used to monitor torsional vibration. The air-gap torque spectrum was used to identify torsional excitation frequencies in the measured torque signal. Measurements from the sensors identified lateral and anisotropic cross-coupling. The magnetostrictive torsional vibration sensors signals agreed with the reference, even though they were installed in a practical but non-ideal location and viewed an exposed part of the shaft that is subject to mechanical abuse. Torsional vibration measurements provided critical insight into the machine behavior that models did not explain.

As torsional monitoring solutions broaden and find wider application, the industry will continue to learn about the interaction between torsional vibration, lateral vibration, and machine faults. This paper presents one possibility of interaction in the expectation that additional interactions and faults can be identified prior to a mechanical failure of a coupling or shaft leading to improved industry understanding of torsional vibration.

NOMENCLATURE

AF	= Amplification factor	(-)	T	= Applied torque	(N-m)
A_{hp}	= Half-power amplitude	(N-m)	U_s	= Stator voltage	(V)
A_r	= Amplitude at resonance	(N-m)	$U_{s,n}$	= Nominal Stator voltage	(V)
B_s	= Stator induction field	(T)	V_h	= Motor harmonics	(V)
c	= Damping	(N-m-s/rad)	Z_h	= Motor impedance	(ohms)
C_f	= Filter capacitance	(F)	Γ	= Torque	(N-m)
f_{in}	= Line-in frequency	(Hz)	Γ_{load}	= Load torque	(N-m)
f_{out}	= Line-out frequency	(Hz)	ξ	= Damping ratio	(-)
f_{PWM}	= Pulse-width modulation frequency	(Hz)	τ_{tq}	= Torsional stress	(MPa)
I_h	= Motor current harmonics	(A)	ω	= Stator field frequency	(rad/s)
I_m	= Magnetization current	(A)	ω_{drive}	= Stator pulsation	(rad/s)
I'_r	= Rotor current on stator referential	(A)	Ω_n	= Nominal rotor speed	(RPM)
I_s	= Stator current	(A)	Ω_r	= Rotational pulsation	(rad/s)
J_p	= Second polar Moment of Inertia	(m ⁴)	Ω_{rs}	= Slippage	(rad/s)
K_i	= Coefficient	(-)			
L_f	= Filter inductance	(H)			
L_m	= Magnetization inductance	(H)			
L'_r	= Rotor inductance on stator referential	(H)			
L_s	= Stator inductance	(H)			
N_1	= Lower frequency at half-power	(CPM)			
N_2	= Upper frequency at half-power	(CPM)			
N_r	= Frequency at resonance	(CPM)			
p	= Number of Pole Pair	(-)			
P_{in}	= Absorbed power	(W)			
P_{js}	= Stator joule losses	(W)			
p_M	= Pulse number of inverter	(-)			
P_m	= Mechanical losses	(W)			
P_{mag}	= Magnetization losses	(W)			
P_{mec}	= Output power	(W)			
P_n	= Nominal power	(W)			
p_s	= Pulse number of rectifier	(-)			
P_{TR}	= Transmitted power	(W)			
q	= Electric charge	(C)			
R_f	= Filter resistance	(ohms)			
R_{Rotor}^{Outer}	= Outer rotor radius	(m)			
R_m	= Magnetization resistance	(ohms)			
R'_r	= Rotor resistance on stator referential	(ohms)			
R_s	= Stator resistance	(ohms)			
s	= Laplace variable	(-)			
$S1$	= Sense pole 1	(-)			
$S2$	= Sense pole 2	(-)			
$S3$	= Sense pole 3	(-)			
$S4$	= Sense pole 4	(-)			
sl	= Slip	(-)			

APPENDIX A

Torsional analysis of VFD systems often focuses on the features of the power system; however, the parameters of the motor ultimately determine how the excitation frequencies interact with the torsional resonances of the system.

The three stator windings create a rotating magnetic field. Its frequency of rotation is called the synchronism frequency. The rotor consists of copper bars not insulated, short-circuited at their end by two conductive rings and constitute a "squirrel cage". The cage is swept by the rotating magnetic field.

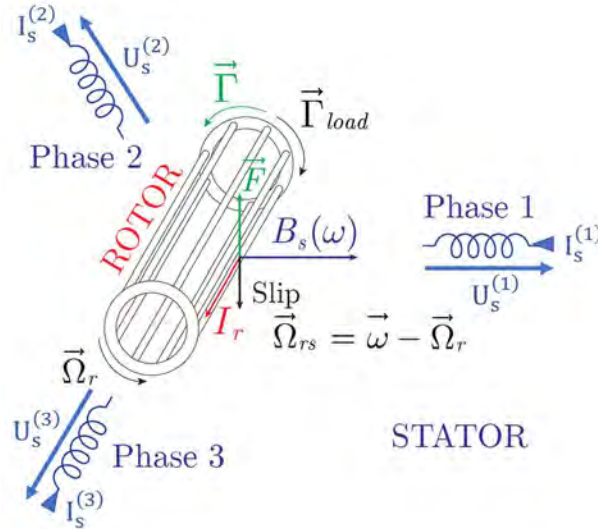


Figure 25 - Principle of torque generation in a squirrel cage induction motor.

When a resistant torque ($\vec{\Gamma}_{load}$) is applied on the shaft by the load, it induces a rotor slippage (Ω_{rs}) with a rotor pulsation (Ω_r) a bit lower than the stator pulsation (ω_{drive}/p) which is fixed by the control of the inverter:

$$\Omega_{rs} = (\omega_{drive}/p) - \Omega_r \quad (1)$$

The slip (sl) is equal to:

$$sl = \Omega_{rs} / \omega_{drive} \quad (2)$$

The Lorentz Force induces the rotor current into the cage:

$$\vec{I}_r = K_1 \cdot q \cdot \vec{\Omega}_{rs} \wedge \vec{B}_s \quad (3)$$

If the rotor turns at exactly the same frequency as the stator field, then no torque is produced. As the rotor speed decreases with respect to the stator electric frequency ("slip") torque is produced. Variation in the current and interaction across harmonics, produce variation in the torque (torsional vibration). The Laplace Force induces the torque generation in opposite to the resistant (load) torque:

$$\vec{\Gamma} = \vec{F} \cdot R_{Rotor}^{Outer} = (K_2 \cdot \vec{I}_r \wedge \vec{B}_s) \cdot R_{Rotor}^{Outer} \quad (4)$$

Variation in the current and interaction across harmonics, produce variation in the torque proportional to $U_s(t) * I_s(t)$. The electromagnetic torque produced in the air-gap of the machine, between the stator and the rotor, can be calculated with the experimental measurement of the stator voltage $U_s^{(k)}(t)$ and current $I_s^{(k)}(t)$ of each phase k where $k \in \{1,2,3\}$ using the equivalent phase circuit of the induction machine described in the Figure 26.

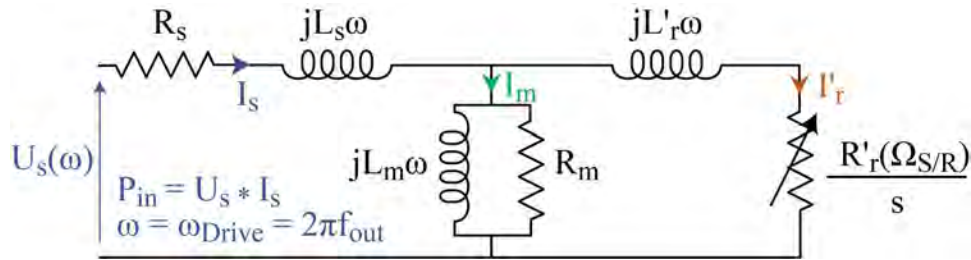


Figure 26 - Induction motor equivalent circuit for one phase

The input power (P_{in}), stator joule losses (P_{js}), and losses of magnetization (P_m) are respectively given as follow:

$$P_{in} = \sum_{k=1}^3 U_s^{(k)}(t) \cdot I_s^{(k)}(t) \quad (5)$$

$$P_{js} = \sum_{k=1}^3 R_s \cdot I_s^{(k)}(t)^2 \quad (6)$$

$$P_m = \sum_{k=1}^3 U_s^{(k)}(t)^2 / R_m \quad (7)$$

The transmitted power is the absorbed power by the electric network from which the losses pertaining to the stator and the magnetization losses are subtracted:

$$P_{TR} = P_{in} - P_{js} - P_m \quad (8)$$

The power transmitted to the rotor is pulled by the load, plus the Joule losses at the rotor, because the rotor iron losses are negligible knowing that the rotor frequency Ω_{rs} at rated load are very low at a maximum of 3Hz, are negligible. We therefore get:

$$P_{jr} = sl \cdot P_{TR} \quad (9)$$

The mechanical power (P_{mec}) is the output power to the load:

$$P_{mec} = (1 - sl) \cdot P_{TR} \quad (10)$$

Thus, the electromagnetic torque in the air gap is equal to:

$$\Gamma_{em} = \frac{P_{mec}}{\Omega_r} = \frac{P_{TR}}{\omega_{drive}} \quad (11)$$

Figure 27 shows the per-phase equivalent circuit with reactance, rather than inductance, values [30]. The torque on the rotor, I_2 , creates the magnetic field and directly relates to torque.

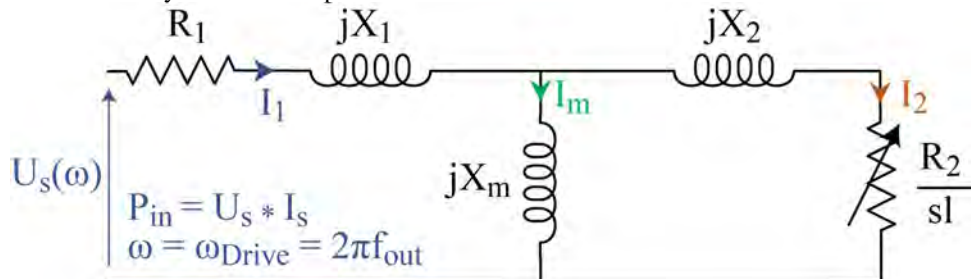


Figure 27 - Equivalent per-phase circuit for induction motor with reactance values.

Since the reason to have a motor is to create torque the usual practice with an equivalent circuit is to reduce it to an expression for input voltage/rotor current (impedance or z), as shown in Equation (12) [30]. Once the impedance has been calculated the current can be estimated for a given voltage input.

$$z = R_1 + iX_1 + \frac{iX_m \left(iX_2 + \frac{R_2}{s} \right)}{iX_m + iX_2 + \frac{R_2}{s}} \quad (12)$$

Table 4 - Drive motor parameters at no load.

	Reactance Values		Inductance Values
Basic Impedance	5.716	Ω - 100 %	
Stator Resistance	0.0380	Ω - 0.66 %	
Stator Leakage Inductance	1.2900	Ω - 22.57 %	4.10620 mH
Rotor Resistance	0.0740	Ω - 1.29 %	
Rotor Leakage Inductance	0.4200	Ω - 7.35 %	1.33690 mH
Magnetic Inductance in charge	43.0000	Ω - 752.2 %	0.13687 H
Magnetic Inductance empty	45.15	Ω - 789.8 %	
Iron loss resistance	1923.0	Ω - 33.64 %	
Leakage capacitance	100	nF	

For the drive motor in this test stand, operating at full-speed and no load (slip = 0.031 or 3.1%), the motor has the properties shown in Table 4. With these parameters the impedance can be found as:

$$z = 8.26 \angle 12.8^\circ \text{ ohms}$$

The current phase is shown relative to the voltage phase so if the voltage is $220/\sqrt{3}$ then current is:

$$i = 15.3 \angle -12.8^\circ \text{ ohms}$$

When it comes to VFD system and torsional interaction the system response is more complicated than a single component. In that case the equivalent circuit is re-cast into a Laplace domain (continuous time or CT) solution:

$$Z = \frac{R_2 + s(sl X_2 + sl X_m)}{R_1 R_2 + s(R_2 X_1 + sl r_1 X_2 + sl r_1 X_m + r_2 X_m) + s^2(sl X_1 X_2 + sl X_1 X_m + sl X_2 X_m)} \quad (13)$$

The continuous time transfer function can be warped to the z-domain by a variety of transformations (bilinear, zero-order hold, impulse sampling, etc.) to obtain a discrete-time (DT) transfer function so that it can apply directly to sampled data [31]. In this case the bilinear transform was used. The analytical results obtained above was then compared to the continuous time (Laplace) and DT systems. Figure 28 shows the results. At the start of the simulation the Laplace and DT systems match each other but differ from the steady-state analytical solution. This is expected behavior as both the CT and DT transfer functions include transient and steady-state response. Once the system settles out, both transfer functions match the analytical results. This gives a good indication that both transfer functions accurately represent system behavior.

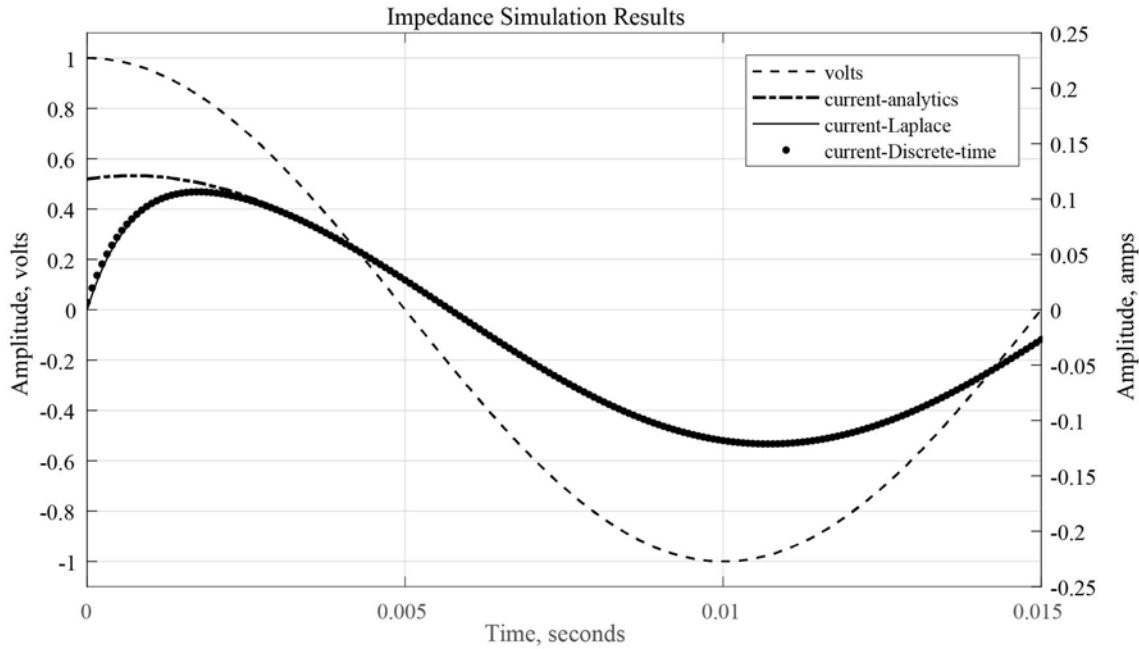


Figure 28 – Analytical, continuous time, and discrete-time simulation results.

With a transfer function defined, the system response (current output to voltage input) can be examined over frequency. Figure 29 shows the amplitude and phase response for rotor current as the motor voltage input frequency changes. From 10 to 1000 hertz the amplitude drops from 400 to less than 100 amps. What is true for this specific motor is generally true for all motors: as the input frequency increases, the current response drops off. This is one of the reasons why torsional vibration frequency greater than 1000 hertz are rarely considered.

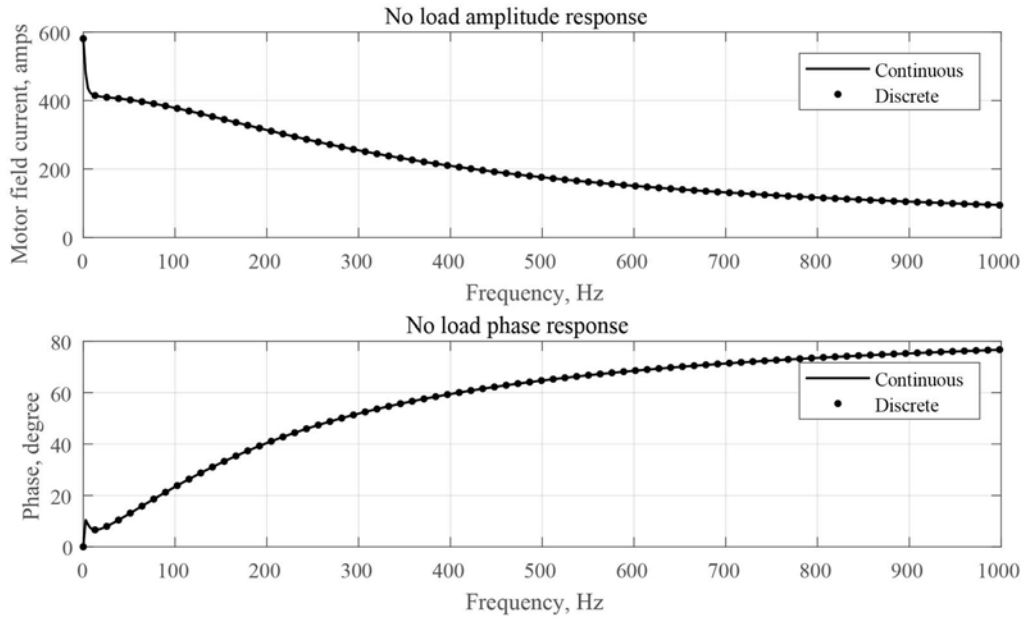


Figure 29 – Motor field current amplitude and phase response as voltage input frequency changes.

The equivalent circuit also shows that as the slip increases, the motor field current increases. This in turn increases the torque generated by the motor. With slip increasing to 4.7% there is less roll-off in the current from 0 to 120 hertz region. Any torsional excitation forces in this region would be more pronounced than if the motor was operating at 3.1% slip. As the frequency increases to 1000 hertz, the 4.7% slip current drops to nearly the same level as the 3.1% current as motor field characteristics dominate the circuit.

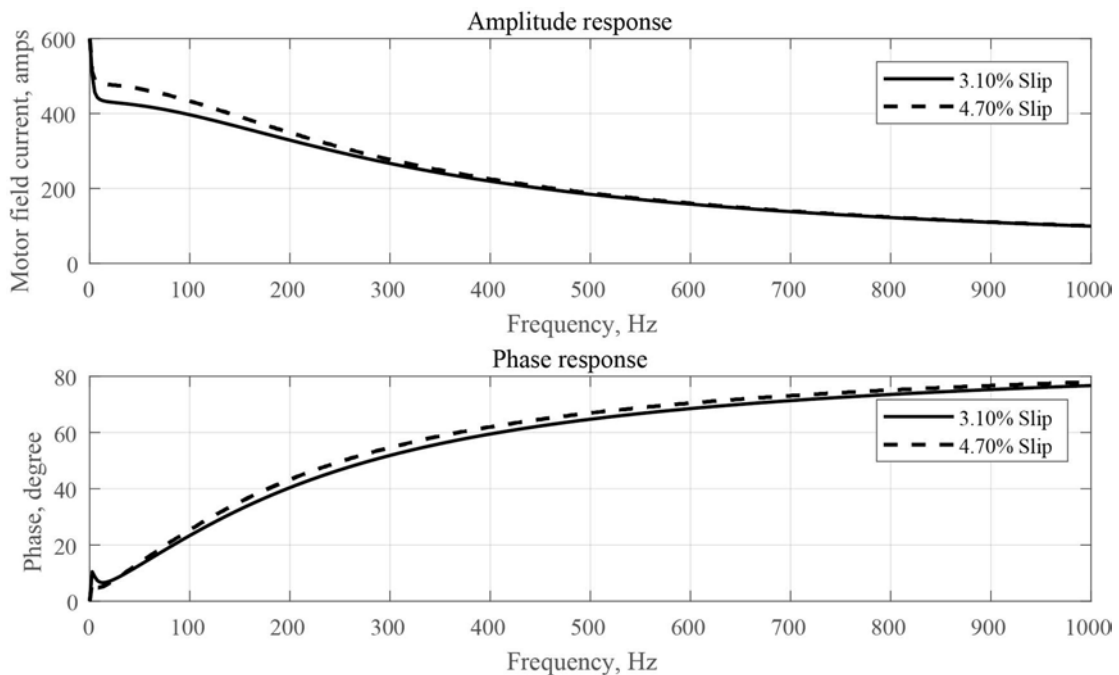


Figure 30 – Motor field current amplitude and phase response as slip changes.

APPENDIX B

This section provides background on the magnetostrictive torsional vibration sensor used in this test stand. Magnetostriction is when a ferromagnetic material, such as iron or nickel, is exposed to an external magnetic field which causes the material to change dimensionally (this effect was first discovered by the English physicist James Joule in 1842 and is the reason transformers sometimes hum due to their alternating magnetic fields [20]). In 1865 Emilio Villari, an Italian physicist, discovered the inverse effect of magnetostriction (also known as the magnetoelastic effect or Villari effect), which describes the change in a material's magnetic susceptibility/permeability due to an applied mechanical stress. The Villari effect has been utilized in sensor development to convert mechanical energy to magnetic energy, which was first done by James Ewing (Scottish physicist and engineer) who made the first magnetostrictive sensor measuring force in 1888 [21].

The magnetoelastic effect enables non-contacting torsional vibration sensors that install and operate without shaft preparation, provide a continuous time signal, and measure a wide range of torque values. Table 5 summarizes the commonly used continuous torsional vibration measurement technologies.

Table 5 - Summary of torsional vibration measurement technologies [22][23][24].

Technology	Installation	Performance
Strain gages	<ul style="list-style-type: none"> • Shaft modification for the gage. Requires specialized knowledge. • Requires wireless power and telemetry system. • Must know the maximum stress prior to installation to select the correct gage factor. • Performance is best when located on compliant shaft string members 	<ul style="list-style-type: none"> • With temperature compensation provides accurate DC and AC measurements. • Can be difficult to maintain good bonding between gage and shaft.
Surface acoustic wave (SAW)	<ul style="list-style-type: none"> • Shaft modification for the resonator. Requires specialized knowledge to bond correctly. • Requires wireless interrogator. 	<ul style="list-style-type: none"> • Accurate DC measurement, requires multiple interrogators for AC measurement. • Can be difficult to maintain good bonding between resonator and shaft.
Demodulation	<ul style="list-style-type: none"> • Shaft modification for toothed wheel 	<ul style="list-style-type: none"> • Accurate AC measurement. Requires precision clocking for DC measurement. • Difficult to measure multiple planes
Magnetostrictive	<ul style="list-style-type: none"> • Installation is like an eddy-current probe – requires bracket and secure mounting to a bearing. • Performance is best when located on compliant shaft string members 	<ul style="list-style-type: none"> • With compensations, accurate AC measurement and an indication of DC torque. • Runout removal restricts transient measurement capability.

In its simplest form a magnetostrictive sensor can be shown as a single-branch element which consists of a C-shaped ferromagnetic core with two coils, as shown in Figure 31. A time-varying drive coil voltage (typically sinusoidal and operating at 1 to 100 kHz), applied to the drive coil, induces magnetic flux in the core which couples to a target material (i.e. 4140 steel) through an air gap. The magnetic flux lines generated by the drive coil must close which requires that most pass through the sense coil, inducing a current. The voltage created by this current passing through the coil resistance can be measured.

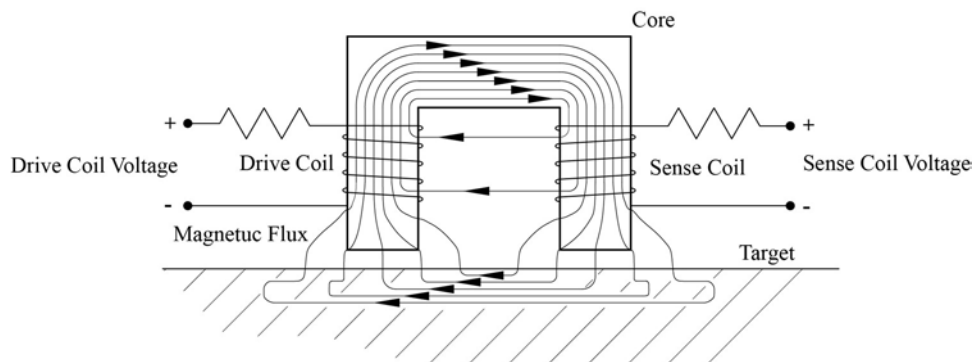


Figure 31 – Schematic of single-branch magnetostrictive sensor.

If stress changes the magnetic properties of a material, then it is called a magnetostrictive material. Magnetic permeability, referred to as permeability in this paper, describes the ability of a material to support a magnetic field and it usually this magnetic property that is of interest in magnetostrictive materials. If the target material in Figure 31 is magnetostrictive then mechanical stresses acting on the target alter the magnetic permeability. The change in permeability alters the lines of magnetic flux which can be detected as changes in the sense coil output.

The magnetostrictive torsional vibration sensor used in this test was a four-branch design. This design places four sense poles at 90° angles around a center drive pole, as illustrated in Figure 32. This design was first described by Beth and Meeks of the Case Western Reserve University in 1954 [25]. This configuration allows the sensor to detect both the tension and compression principle stresses that occur helically at 90° from each other, as shown in Figure 32. This arrangement induces a nearly circular magnetic field in the target, shown by the model in the right side of Figure 32, when the shaft is homogeneous and in the neutral state.

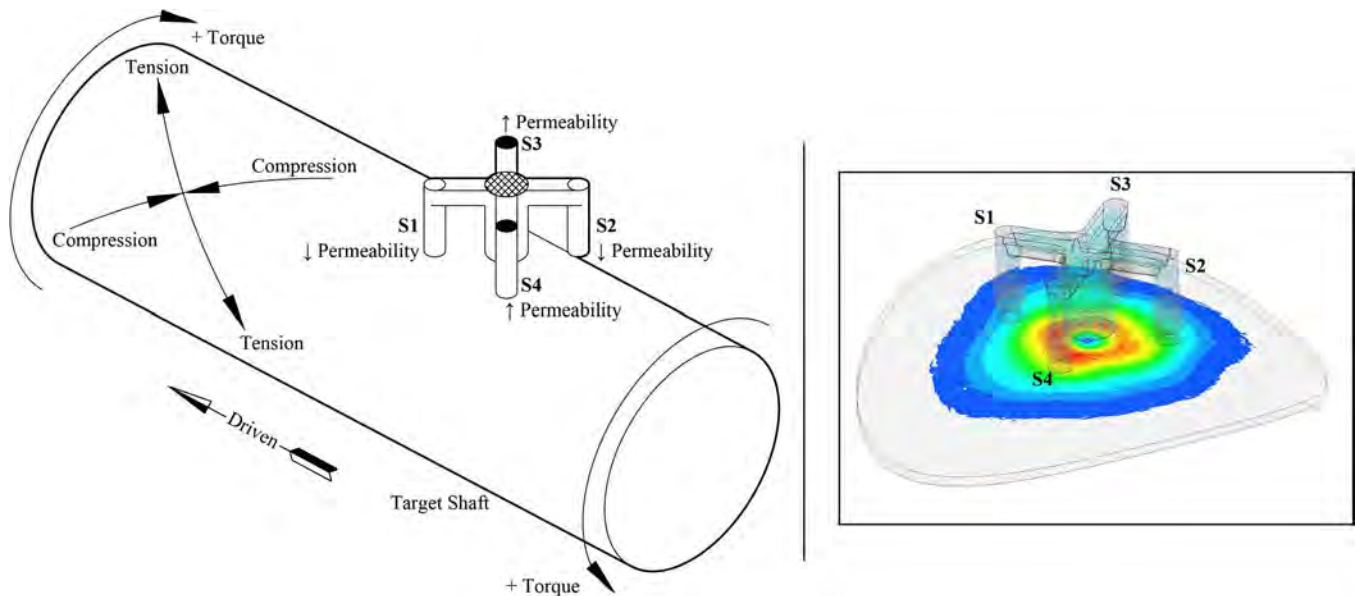


Figure 32 – Four-branch magnetostrictive sensor and stress schematic on round target under pure torsional loading (left side). Core and magnetic lines of flux when viewing a round target (right side).

When the shaft is in a neutral state, the permeability is uniform; therefore, the magnetic flux flows evenly through all four sense poles creating a balanced output. When pure torque is applied to the shaft in the positive direction (counter-clockwise as viewed from the driver to driven and as shown in Figure 32) the principal stress sense between sense pole 1 (S1 in Figure 32) and sense pole 2 (S2 in Figure 32) is in compression. Compressive stress causes the permeability and magnetic flux to decrease so the sense pole voltages decrease with increasing compressive stress as shown in quadrants III and IV of Figure 33. Conversely the principal stress through sense pole 3 (S3 in Figure 32) and sense pole 4 (S4 in Figure 32) is in tension, causing the permeability and magnetic flux to increase. Increasing stress raises their sense pole voltage, as shown in quadrants I and II of Figure 33. The compression sense pole voltages, which dropped and are negative with respect to the neutral material state, are subtracted from the tension sense pole voltages:

$$S3 + S4 - (S1 + S2) = \text{Raw Full Bridge} \quad (14)$$

Taking the difference of the summed poles from each principle stress line increases the overall sensitivity while also providing excellent common mode noise rejection for both external sources as well as the driver circuit. The four-branch arrangement also provides for rejection of bending stresses when they act on the shaft. This summation, using (14), of sense pole voltages generates the raw full bridge output shown in Figure 34. A gain on offset are applied to this raw output to arrive at the gap full bridge output.

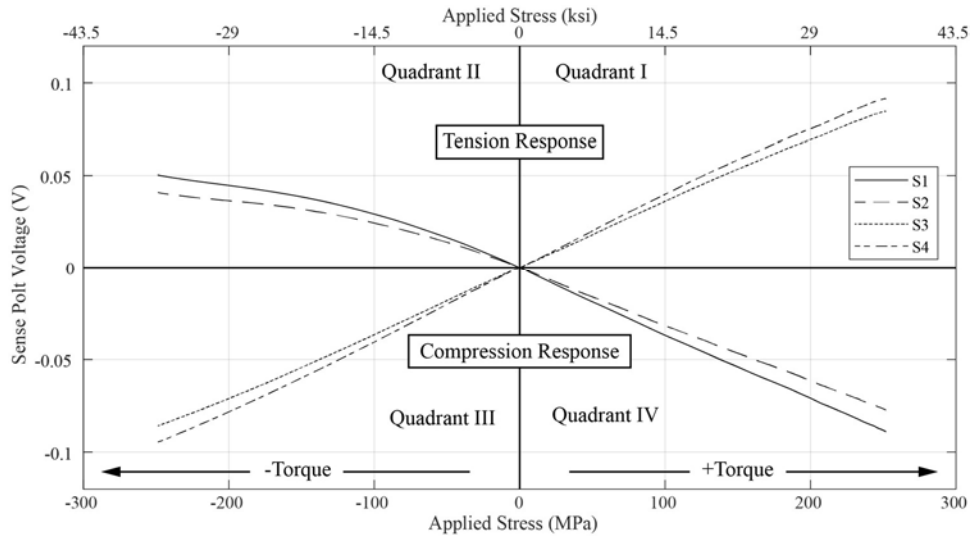


Figure 33 - Sense pole response as target stress changes on a 4140 target. Positive torque follows the convention of Figure 32.

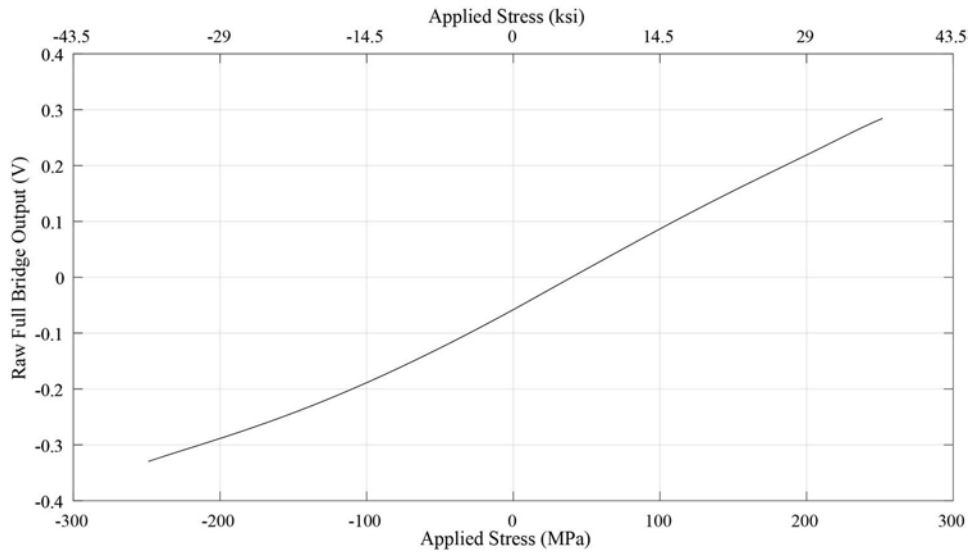


Figure 34 – Raw full bridge response as target stress changes.

Sensitivity Over Gap

As the air gap between the probe and target shaft increases, air-gap permeance decreases which decreases the magnetic flux coupled through the target. The drop in magnetic flux causes the sensitivity to stress to decrease as well since there is less magnetic field passing through the target. Air gap effect on the sensor was tested from 0.020” to 0.070”, shown in Figure 35, which illustrates the sensitivity over gap is linear and decreased by approximately 33% over the 0.050” range. To allow visibility to the details in the different curves just the positive (tensile) portion is shown; however, the negative side behaves similarly.

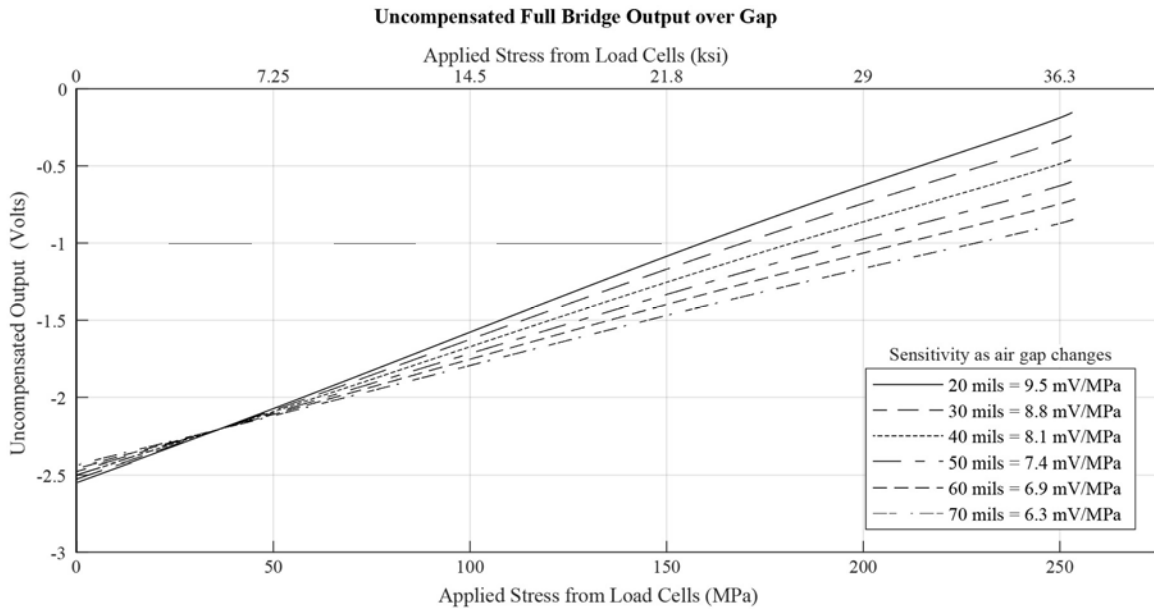


Figure 35 – Uncompensated full bridge output.

An offset error is also shown in Figure 35, which is due to asymmetries in the sense pole outputs over air gap caused by various inhomogeneity in the shaft. The inhomogeneity can be caused by residual stresses due to machining, magnetism, and probe alignment. To compensate for gain and offset errors over gap, an offset correction is applied to collapse the zero-stress sensor output to zero volts over gap. Then a gain compensation is applied to maintain a constant 25mV/MPa sensitivity over gap range. The gap compensated full bridge signal is shown below in Figure 36.

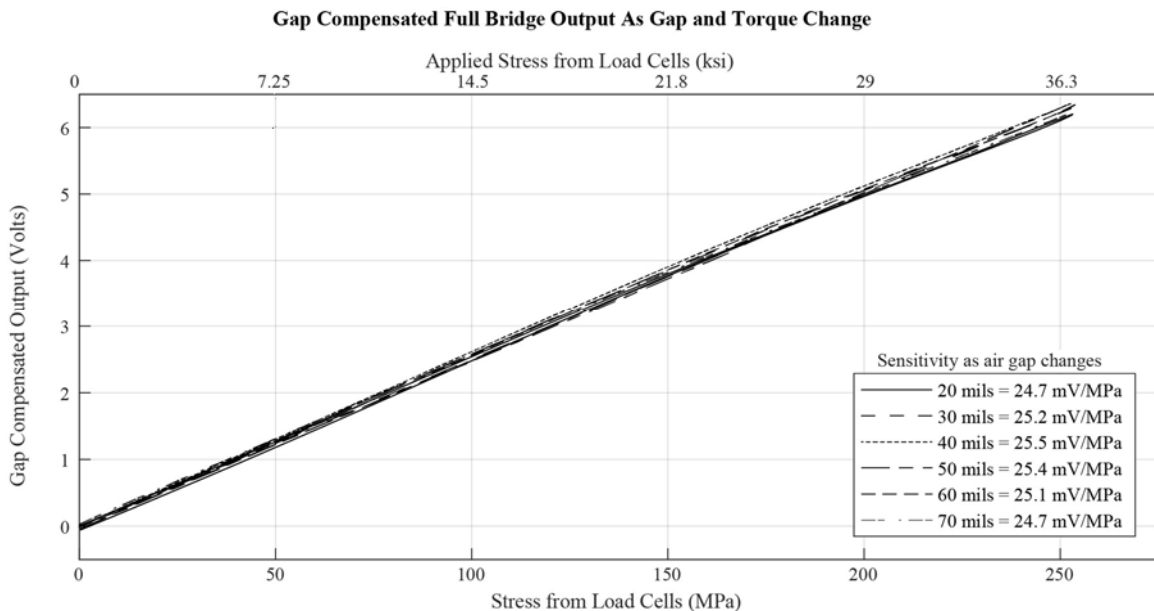


Figure 36 – Gap compensated full bridge output.

Material and Runout

Like eddy-current probes, magnetostrictive torsional vibration sensors respond to material inhomogeneities resulting in signal content not related to torsional vibration as the shaft turns. Magnetostrictive sensors require many of the same considerations as do eddy-current probes during installation. Magnetostrictive sensors require calibration to the target material; however, they are limited to magnetostrictive target shaft materials, such as iron and nickel. They are also highly sensitive to electrical runout, sideview, and crosstalk.

Crosstalk describes interference between two sensors placed close to each other. If the drive frequencies are similar, then a beat frequency (the difference between the two drive frequencies) appears in the output of both sensors. Since some compensation methods use two probes near each other their drive frequencies were shifted relative to one another such that the crosstalk beat frequency was above the desired frequency response.

Uncompensated electrical runout in the target shaft material can account for a significant portion of the sensor's full-scale signal of 300 MPa. Runout describes a condition in which inhomogeneities in the shaft (surface imperfections, localized stresses, etc.) create a change in the magnetic permeability of the shaft which generates a signal that is not related to torque (it does not refer to changes in the sensor signal due to gap changes). Like an eddy current probe this effect is reduced by degaussing and burnishing the shaft. While shot peening reduces electrical runout it also reduces stress sensitivity, making the process less effective [21].

Since runout can never be fully removed from the shaft, several methods of compensation were tested. One approach measured and stored the runout pattern as the shaft turned under no-load conditions ("zero stress waveform compensation"). While zero stress waveform compensation of the shaft is effective in the short term it exhibits too much variability over time, stress, temperature, and changes in axial shaft location to be an effective solution.

The method used in this paper applies two probes per measurement plane in conjunction with a Keyphasor and is referred to as dual probe runout compensation. This technique uses an algorithm to differentiate the runout and torque signal using the observation that torque arrives simultaneously at each probe, but that runout pattern is delayed between the two magnetostrictive sensors due to the shaft rotation that carries the pattern from one probe to the next.

Figure 37 shows the runout observed in this test stand. The magnetostrictive probe viewed an exposed and unconditioned portion of the shaft. The runout, shown by the dashed lines in Figure 37, was reduced an order of magnitude from approximately 7.5 volts peak-to-peak [300 MPa / 44 ksi] to 0.7 volts peak-to-peak [28 MPa / 4 ksi]. With additional techniques, such as spectral averaging, torsional signals as low as 0.05 mV [0.002 MPa / 0.3 psi] can be detected.

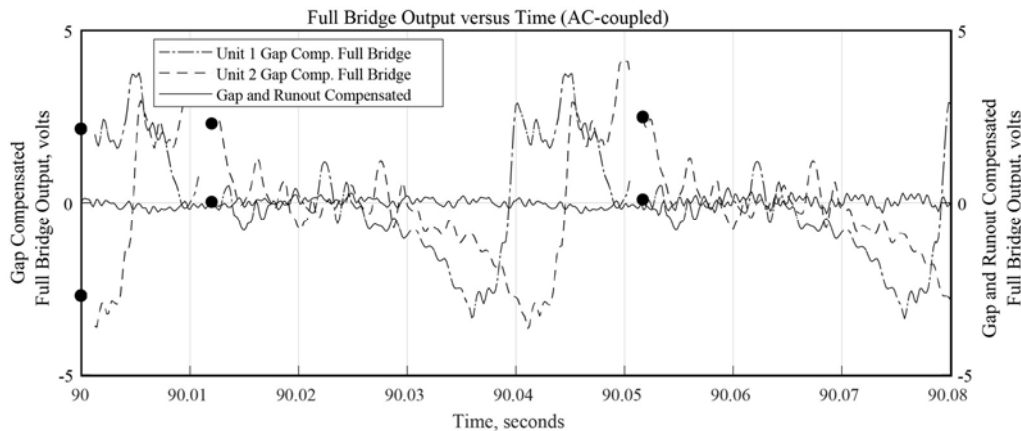


Figure 37 – Gap and runout full bridge compensation signals as test string rotates.

The voltage signal of the magnetostrictive torsional vibration sensor indicates the surface stress in the sensor viewing area. As described in Appendix this surface stress relates to the torque in the viewed section of the shaft as:

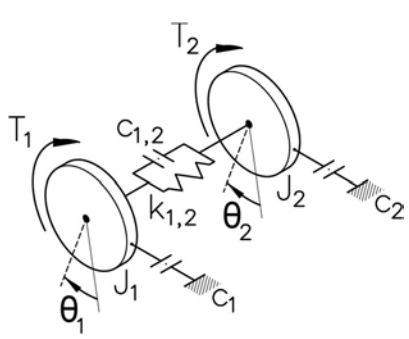
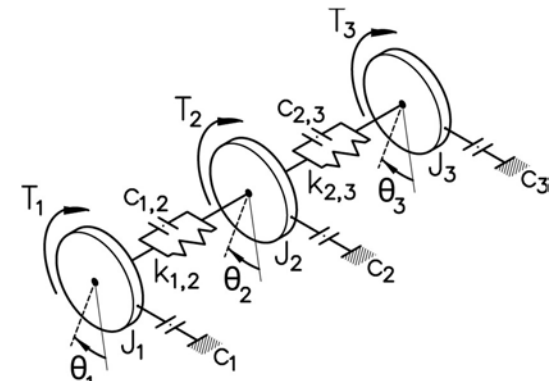
$$T = \frac{\pi}{2} (\tau_{tq,max}) * (\rho_{outer}^3) \quad (15)$$

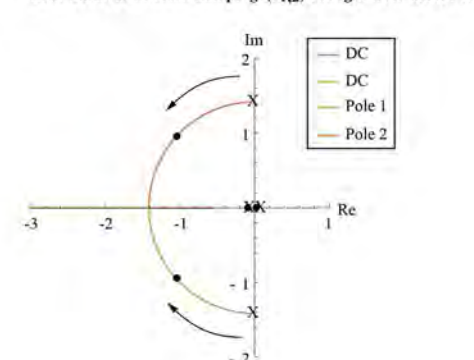
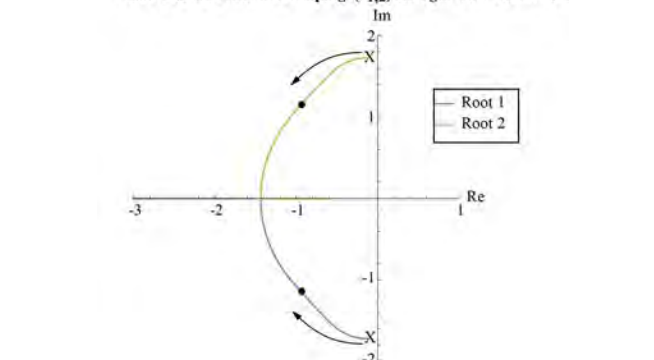
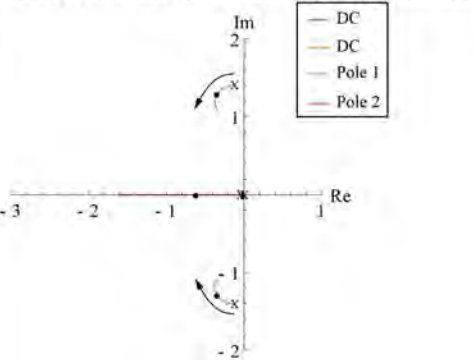
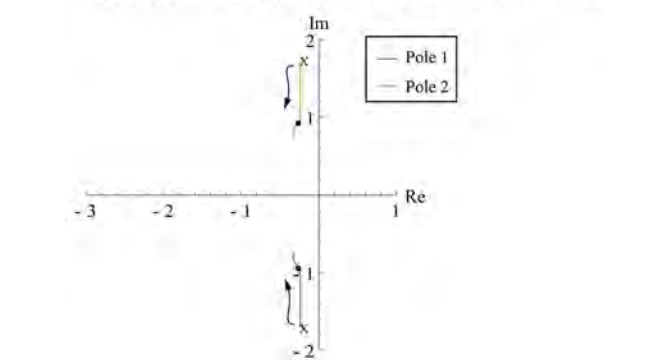
APPENDIX C

The torsional model used in this paper includes internal damping. Development of such models is well covered in industry. While not difficult, the model development involves quite a few variables. For reference this section presents fully developed models, with both internal and external damping, and transfer functions for a 2- and 3-mass system. These transfer functions can be reduced to exclude external damping by setting the external damping variables (c_1 , c_2 , and c_3) to zero. The fully developed models in this appendix describe how changes in external and internal damping effect the pole migration system response.

Table 6 summarizes the 2- and 3-mass models. The order-reduced state-space matrices can readily be extended to higher order systems such as the one in this paper. A variety of tools, most of them free, can be used to analyze these systems. These tools include MATLAB, Python, Scilab, and Mathematica.

Table 6 - Two- and Three- mass models with internal and external damping.

	2-mass system	3-mass system
Sketch		
Nomenclature	θ_1, θ_2 Angular displacement, radian T_1, T_2 Applied torque, N-m J_1, J_2 Polar mass moment of inertia (MR^2) c_1, c_2 External (inertial) damping, N-m-s/rad $c_{1,2}$ Internal damping, N-m-s/rad $k_{1,2}$ Stiffness, N-m/rad	$\theta_1, \theta_2, \theta_3$ Angular displacement, radian T_1, T_2, T_3 Applied torque, N-m J_1, J_2, J_3 Polar mass moment of inertia (MR^2) c_1, c_2, c_3 External (inertial) damping, N-m-s/rad $c_{1,2}, c_{2,3}$ Internal damping, N-m-s/rad $k_{1,2}, k_{2,3}$ Stiffness, N-m/rad
Characteristic Equation (Free Vibration)	$s^4 J_1 J_2 + s^2 (J_1 k_{1,2} + J_2 k_{1,2}) = 0$	$q_b s^2 + 2q_a s^4 + s^6 = 0$ $q_b = \frac{(J_1 + J_2 + J_3)k_{1,2}k_{2,3}}{J_1 J_2 J_3}$ $q_a = \frac{(J_1 + J_2)k_{1,2}}{2J_1 J_2} + \frac{(J_2 + J_3)k_{2,3}}{2J_2 J_3}$
Roots (Free Vibration)	$\frac{\sqrt{J_1 + J_2} \sqrt{k_{1,2}}}{\sqrt{J_2 J_1}}$	$\sqrt{-q_a - \sqrt{q_a^2 - q_b}}, \sqrt{-q_a + \sqrt{q_a^2 - q_b}}$

<p>State-space A matrix</p>	$\begin{bmatrix} 0 & 0 & 1 & 0 \\ 0 & 0 & 0 & 1 \\ -\frac{k_{1,2}}{J_1} & \frac{k_{1,2}}{J_1} & -\frac{c_1}{J_1} - \frac{c_{1,2}}{J_1} & \frac{c_{1,2}}{J_1} \\ \frac{k_{1,2}}{J_2} & -\frac{k_{1,2}}{J_2} & \frac{c_{1,2}}{J_2} & -\frac{c_2}{J_2} - \frac{c_{1,2}}{J_2} \end{bmatrix} \begin{bmatrix} \theta_1[t] \\ \theta_2[t] \\ \theta_1'[t] \\ \theta_2'[t] \end{bmatrix}$ $q1 = -\frac{c_1}{J_1} - \frac{c_{1,2}}{J_1}, q2 = -\frac{c_2}{J_2} - \frac{c_{1,2}}{J_2}$	$\begin{bmatrix} 0 & 0 & 0 & 1 & 0 & 0 \\ 0 & 0 & 0 & 0 & 1 & 0 \\ 0 & 0 & 0 & 0 & 0 & 1 \\ -\frac{k_{1,2}}{J_1} & \frac{k_{1,2}}{J_1} & 0 & q1 & \frac{c_{1,2}}{J_1} & 0 \\ \frac{k_{1,2}}{J_2} & -\frac{k_{1,2}}{J_2} - \frac{k_{2,3}}{J_2} & \frac{k_{2,3}}{J_2} & \frac{c_{1,2}}{J_2} & q2 & \frac{c_{2,3}}{J_2} \\ 0 & \frac{k_{2,3}}{J_3} & -\frac{k_{2,3}}{J_3} & 0 & \frac{c_{2,3}}{J_3} & q3 \end{bmatrix} \begin{bmatrix} \theta_1[t] \\ \theta_2[t] \\ \theta_3[t] \\ \theta_1'[t] \\ \theta_2'[t] \\ \theta_3'[t] \end{bmatrix}$ $q1 = -\frac{c_1}{J_1} - \frac{c_{1,2}}{J_1}, q2 = -\frac{c_2}{J_2} - \frac{c_{1,2}}{J_2} - \frac{c_{2,3}}{J_2}, q3 = -\frac{c_3}{J_3} - \frac{c_{2,3}}{J_3}$
<p>Eigenvalue migration as internal damping changes</p>	<p>Root Locus as internal damping ($c_{1,2}$) changes from 0.0001 to 2</p> 	<p>Root Locus as internal damping ($c_{1,2}$) changes from 0.0001 to 2</p> 
<p>Eigenvalue migration as external damping changes</p>	<p>Root Locus as external damping at mass 1 (c_1) changes from 0.0001 to 2</p> 	<p>Root Locus as external damping at mass 1 (c_1) changes from 0.0001 to 2</p> 

APPENDIX D

Magnetostrictive sensors respond to stress in the shaft. To convert the measured stress to a torque, the properties of the shaft section viewed by the magnetostrictive sensor must be considered. As described previously, a shaft in torsion experiences tensile and compressive stresses that occur helically at 90° from each other (See Figure 32). These stresses are proportional to the shaft radius, ρ , applied torque, T , divided by the second polar moment of inertia, J_p [32]:

$$\tau_{tq} = \frac{T \rho}{J_p} \quad (16)$$

For reference, Figure 38 shows the nomenclature applied to a solid cylindrical section.

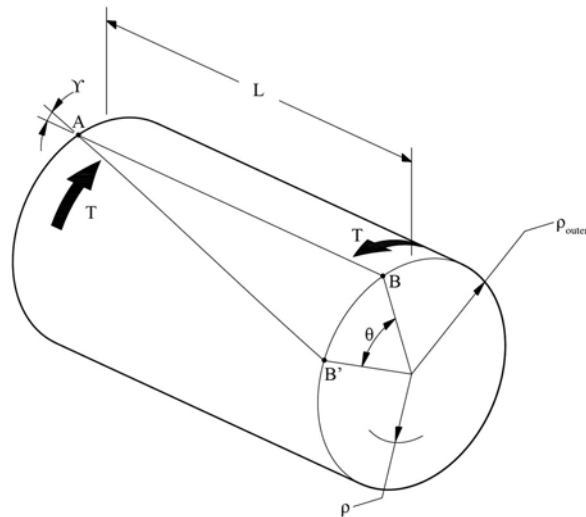


Figure 38 - Surface stress to torque.

If all has gone well in the fabrication process then turbomachinery rotors are cylindrical. The magnetostrictive torsional vibration sensor only sees the outer most stresses (surface stresses) of the shaft. If the shaft is solid, then these two observations can be combined to produce a simplified relationship between stress and torque:

$$T = \frac{\pi}{2} (\tau_{tq,max}) * (\rho_{outer}^3) \quad (17)$$

In terms of torque, T , the stress at the surface, $\tau_{tq,max}$, can be found as:

$$\tau_{tq,max} = \frac{T}{\rho_{outer}^3} \frac{2}{\pi} \quad (18)$$

APPENDIX E

Damping can be measured from the bode plots of torsional forcing function to torsional response. Unlike lateral vibration, in which the forcing function is almost always a rotating unbalance, the forcing function may or may not be related to running speed. In this case, for coast-down, both drive motor and load motor rotors are anisotropic and heavy so that the lateral vibration cross-couples into the torsional vibration.

Both the 2-pole drive motor field and 4 pole load motor field provide torsional excitation. The drive motor field is anisotropic and loaded by gravity, shown in Figure 39, with two large bars that create a 2X torsional forcing function. This forcing function dominates on the machine coast down.

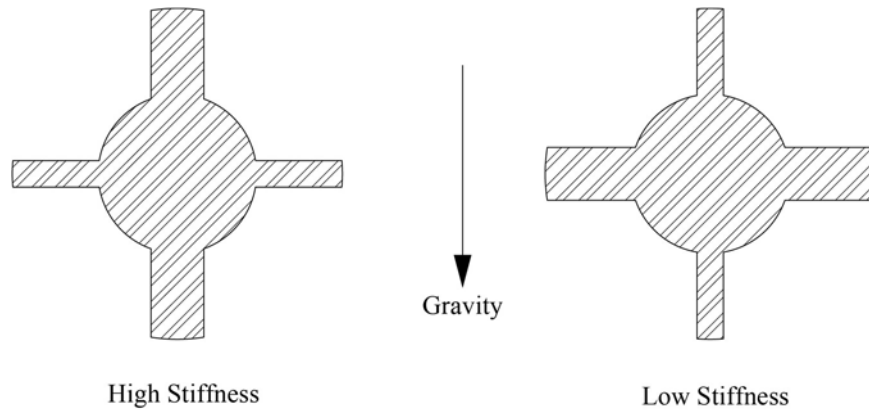


Figure 39 – Drive motor field cross-section outline

Figure 40 shows the 2X filtered response during a coast down. The top pane shows a resonant response at 732 RPM. This equates to a forcing frequency of 24.4 Hz [1464 CPM]. This is close to the estimated value of 26.4 Hz [1476 CPM] shown in Figure 9 and Figure 11.

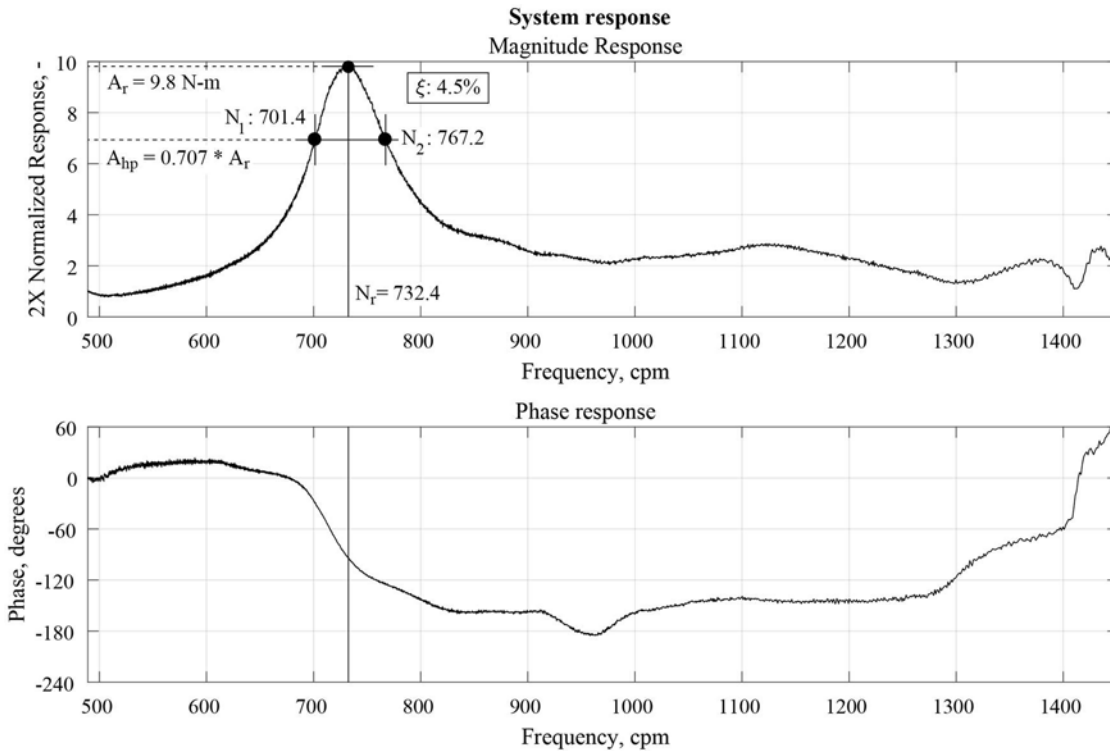


Figure 40 - 2X Filtered coast down torsional response.

For this first mode response the damping can be found following the half-power bandwidth procedure outlined in [17]. First the peak resonant frequency is identified. As damping increases peaks become less defined so location of the 90° phase shift can be helpful in identifying the resonance frequency. As mentioned above this frequency is 12.2 Hz [732 CPM]. Next, the half-power point is calculated as:

$$A_{hp} = 0.707 * A_r \quad (19)$$

This is the short line drawn across the resonance at 7 N-m in Figure 40. The crosses the resonance at two points, labelled N_1 and N_2 in Figure 40. The amplification factor, AF , can be calculated from these two frequencies and the resonant frequency as:

$$AF = \frac{N_r}{N_2 - N_1} = \frac{732.4}{767.2 - 701.4} = 11.1 \quad (20)$$

Torsional systems often refer to damping in terms of fraction of critical damping, ξ , which relates to the amplification factor as:

$$\xi = \frac{1}{2 AF} = \frac{1}{(2) (11.1)} \approx 4.5\% \quad (21)$$

This value is higher than external damping cited in [11]. For a single degree of freedom system, the damping, c , is

$$c = \xi 2 \sqrt{km} \quad (22)$$

Since this is the first mode the machine train can be reduced to an equivalent two-mass system and damping is found to be 780 N-m-s/rad [6900 in-lbf-s/rad].

REFERENCES

- [1] Weber, William J.; Cuzner, Robert M.; Ruckstadter, Eric J.; Smith, Jim (2002). Engineering Fundamentals Of Multi-MW Variable Frequency Drives - How They Work, Basic Types, And Application Considerations.. Texas A&M University. Turbomachinery Laboratories. Available electronically from <http://hdl.handle.net/1969.1/163309>.
- [2] Feese, Troy; Maxfield, Ryan (2008). Torsional Vibration Problem with Motor/ID Fan System Due to PWM Variable Frequency Drive. Texas A&M University. Turbomachinery Laboratories. Available electronically from <http://hdl.handle.net/1969.1/163140>.
- [3] Corcoran, J. P., Kocur, J.A. and Mitsingas, M. C., 2010, "Preventing Undetected Train Torsional Oscillations," *Proceedings of the Thirty-Ninth Turbomachinery Symposium*, Turbomachinery Laboratory, Texas A&M University, College Station, Texas, pp. 135-146.
- [4] Smith, Natalie; Wilkes, Jason; Allison, Timothy; Moore, J. Jeffrey; Kulhanek (2018). Troubleshooting of Sub-synchronous Torsional Interaction Phenomena on an Electric Motor-Driven Centrifugal Compressor. Texas A&M University. Turbomachinery Laboratories.
- [5] Smith, Patrick. "Reciprocating Compressor Failure Due to Torsional Vibration". EnergyTech. March, 2011.
- [6] Adachi, Akira; Murphy, Brian (2016). Torsional Instability of Cooling Tower Fan During Induction Motor Startup. Texas A&M University. Turbomachinery Laboratories.
- [7] Feese, Troy; Kokot, Aleksander (2016). Electromagnetic Effects on The Torsional Natural Frequencies Of An Induction Motor Driven Reciprocating Compressor With A Soft Coupling. Turbomachinery Laboratories, Texas A&M Engineering Experiment Station. Available electronically from <http://hdl.handle.net/1969.1/159789>.
- [8] Atkins, Ken; Clark, James (2017). Torsional Failure on Reciprocating Compressor Package. Turbomachinery Laboratory, Texas A&M Engineering Experiment Station. Available electronically from <http://hdl.handle.net/1969.1/166823>.
- [9] Aho, Tuomo; Nerg, Janne; Baum, Christopher (2017). Torsional Excitation Upon Short-Circuit in Induction Motors - In Conventional and High-Speed Trains. Turbomachinery Laboratory, Texas A&M Engineering Experiment Station. Available electronically from <http://hdl.handle.net/1969.1/166784>.
- [10] Weber, William J.; Cuzner, Robert M.; Ruckstadter, Eric J.; Smith, Jim (2002). Engineering Fundamentals Of Multi-MW Variable Frequency Drives - How They Work, Basic Types, And Application Considerations.. Texas A&M University. Turbomachinery Laboratories. Available electronically from <http://hdl.handle.net/1969.1/163309>.
- [11] Terens, Lucien; Grgic, Andrej (1996). Applying Variable Speed Drives With Static Frequency Converters To Turbomachinery.. Texas A&M University. Turbomachinery Laboratories. Available electronically from <http://hdl.handle.net/1969.1/163440>.
- [12] S. D. Robertson, K. Hebbar, "Torque pulsations in induction motors with inverter drives", IEEE Trans. on Industry and General Applications, vol. IGA-7, pp. 318-323, Mar./Apr. 1971.
- [13] Durantay, Lionel; Taillardat, Jean-Marc; Pradurat, Jean-François; Velly, Nicolas (2018). State of the art for full electric driven refrigeration compressors solutions using adjustable speed drive: which combination of technology leads to the best CAPEX and OPEX solution up to 100MW? in IEEE Transactions on Industry Application, Vol.54, n°3, pp. 2992-3004.
- [14] Durantay, Lionel; Alban, Thomas; Siala, Samy; Billaud, Antoine (2018). Selection and Tests of Innovative Variable Speed Motor-Compressor Solutions for a 55MW Full Electric Off-shore Platform Maximizing Availability and Efficiency with Better Environmental Impact. in IEEE PCIC Conference Record, 2018, Cincinnati.
- [15] Corbo, Mark A.; Melanoski, Stanley B. (1996). Practical Design Against Torsional Vibration.. Texas A&M University. Turbomachinery Laboratories. Available electronically from <http://hdl.handle.net/1969.1/163448>.

- [16] D. J. Sheppard, "Torsional vibration resulting from adjustable-frequency AC drives," in IEEE Transactions on Industry Applications, vol. 24, no. 5, pp. 812-817, Sept.-Oct. 1988. doi: 10.1109/28.8984
- [17] API Standard RP 684, 2005, "API Standard Paragraphs Rotordynamic Tutorial: Lateral Critical Speeds, Unbalance Response, Stability, Train Torsionals, and Rotor Balancing," Second Edition, American Petroleum Institute, Washington, D.C
- [18] Brown, Royce N. (1984). Torsional-Damping-Transient and Steady State. Texas A&M University. Turbomachinery Laboratories. Available electronically from <http://hdl.handle.net/1969.1/163659>.
- [19] Hutten, Volker; Krause, Tim; Ganesan, Vijay Anantham; Beer, Christian; Demmig, Sven (2013). VSDS Motor Inverter Design Concept for Compressor Trains Avoiding Interharmonics in Operating Speed Range and Verification. Texas A&M University. Turbomachinery Laboratories. Available electronically from <http://hdl.handle.net/1969.1/162922>.
- [20] Joule, J.P. (1847). "On the Effects of Magnetism upon the Dimensions of Iron and Steel Bars". The London, Edinburgh, and Dublin Philosophical Magazine and Journal of Science. 30, Third Series: 76–87, 225–241. Retrieved 2009-07-19.
- [21] Fleming, W., "Magnetostrictive Torque Sensors — Derivation of Model," SAE Technical Paper 890482, 1989.
- [22] Vance JM, French RS. Measurement of Torsional Vibration in Rotating Machinery. ASME. J. Mech., Trans., and Automation. 1986;108(4):565-577. doi:10.1115/1.3258771.
- [23] Wachel, J. C. (Buddy); Szenasi, Fred R. (1993). Analysis Of Torsional Vibrations In Rotating Machinery.. Texas A&M University. Turbomachinery Laboratories. Available electronically from <http://hdl.handle.net/1969.1/163506>.
- [24] Fleming, W., "Automotive Torque Measurement: A Summary of Seven Different Methods," IEEE Transactions on Vehicular Technology, Vol.VT-31, No.3, August 1982.
- [25] Fleming, W., "Engine Sensors: State of the Art," SAE Technical Paper 820904, 1982, <https://doi.org/10.4271/820904>.
- [26] Muszynska, A., Goldman, P. and Bently, D. E., 1992, "Torsional/Lateral Cross-Coupled Responses Due to Shaft Anisotropy: A New Tool in Shaft Crack Detection", I. Mech. E., C432-090, Bath, United Kingdom, pp. 257-262.
- [27] Bently, Donald and Hatch, Charles. *Fundamentals of Rotating Machinery Diagnostics*. Bently Pressurized Bearing Press, Canada.
- [28] Kulhanek CD, James SM, Hollingsworth JR. Stiffening Effect of Motor Core Webs for Torsional Rotordynamics. ASME. Turbo Expo: Power for Land, Sea, and Air, Volume 7: Structures and Dynamics, Parts A and B (:):721-729. doi:10.1115/GT2012-69967.
- [29] Nestorides, E.J., 1958, *A Handbook on Torsional Vibration*, Cambridge University Press, Cambridge, UK.
- [30] Nasar, Syed, 1984, *Electric Machines and Transformers*, Macmillan Publishing Company, New York, USA.
- [31] Oppenheim, Alan; Schafer, Ronald, 2010, *Discrete Time Signal Processing*. Third. Upper Saddle River, NJ: Pearson Higher Education, Inc.
- [32] Budynas, Richard G. and Nisbett, J. Keith. *Shigley's Mechanical Engineering Design*, 9th ed., McGraw-Hill Education, 2008, pp. 101–110.

ACKNOWLEDGEMENTS

Special thanks to Clément Biri *Technologist Electrical Engineer* and Sami Siala *System & Drive Consulting Engineer* for their aid in development of the air gap torque model and to Joseph Whitely, *Senior Mechanical Engineer* for his work in developing the Maxwell model for the magnetostrictive torsional vibration sensor core.